Slow particle remineralization, rather than suppressed disaggregation, drives efficient flux transfer through the Eastern Tropical North Pacific Oxygen Deficient Zone

30 October 2021

Jacob A. Cram[1,] Clara A. Fuchsman[1], Megan E. Duffy[2], Jessica L. Pretty[3], Rachel M. Lekanoff[3], Jacquelyn A Neibauer[2], Shirley W. Leung[2], Klaus B. Huebert[1], Thomas S. Weber[4], Daniele Bianchi[5], Natalya Evans[6], Allan H. Devol[2], Richard G. Keil[2], Andrew M.P. McDonnell[3]

[1]Horn Point Laboratory, University of Maryland Center for Environmental Science, Cambridge, MD, USA.

[2]School of Oceanography, University of Washington Seattle, Seattle, WA, USA.

[3]College of Fisheries and Ocean Sciences, University of Alaska Fairbanks, Fairbanks, AK, USA.

[4]School of Arts and Sciences, University of Rochester, Rochester, NY, USA.

[5]Department of Atmospheric and Oceanic Sciences, University of California Los Angeles, Los Angeles, CA, USA.

[6]Department of Biological Sciences, University of Southern California, Los Angeles, CA, USA.

1 Key Points

The upper mesopelagic of the oligotrophic Eastern Tropical North Pacific Oxygen Deficient Zone (ODZ) has low flux attenuation.

Comparison of particle size observations to models suggests that the breakdown of particles of all sizes is slow throughout the ODZ.

Zooplankton appear to transport organic matter into, and disaggregate particles within, the ODZ above 500 m.

2 Abstract

24

25 Models and observations suggest that particle flux attenuation is lower across the mesopelagic zone of

26 anoxic environments compared to oxic environments. Flux attenuation is controlled by microbial

27 metabolism as well as aggregation and disaggregation by zooplankton, all of which also shape the relative

28 abundance of differently sized particles. Observing and modeling particle spectra can provide information

29 about the contributions of these processes. We measured particle size spectrum profiles at one station in

30 the oligotrophic Eastern Tropical North Pacific Oxygen Deficient Zone (ETNP ODZ) using an

31 underwater vision profiler (UVP), a high-resolution camera that counts and sizes particles. Measurements

32 were taken at different times of day, over the course of a week. Comparing these data to particle flux

33 measurements from sediment traps collected over the same time-period allowed us to constrain the

34 particle size to flux relationship, and to generate highly resolved depth and time estimates of particle flux

35 rates. We found that particle flux attenuated very little throughout the anoxic water column, and at some

36 time-points appeared to increase. Comparing our observations to model predictions suggested that

37 particles of all sizes remineralize more slowly in the ODZ than in oxic waters, and that large particles

38 disaggregate into smaller particles, primarily between the base of the photic zone and 500 m. Acoustic

39 measurements of multiple size classes of organisms suggested that many organisms migrated, during the

40 day, to the region with high particle disaggregation. Our data suggest that diel-migrating organisms both

41 actively transport biomass and disaggregate particles in the ODZ core.

3 Plain Language Summary

42

43 Marine snow are microscopic particles that form in the surface of the ocean and sink into the deep ocean.

44 Most of these particles are the remains of dead algae and feces of tiny animals (zooplankton). The deeper

45 the particles sink into the ocean before microbes or animals consume them, the longer it takes before the

46 carbon in those particles can return to the atmosphere. In parts of the ocean where there is no oxygen,

47 more particles sink to greater depths, for reasons that are not well-understood. We used an underwater

48 camera to observe marine snow particles in the ocean just west of Mexico where there is little to no

49 oxygen at depth. We compared the observations to predictions from several computer simulations

50 representing hypothesized mechanisms to explain why particles are consumed less in water without

51 oxygen. Our measurements suggest that one reason that particles sink to deeper depths here is because

52 microbes consume the particles slowly when there is no oxygen. Meanwhile, zooplankton still break large

53 particles into smaller ones and produce fecal pellets in these low oxygen waters.

2

4 Introduction

55 The biological pump, in which sinking microaggregate (< 500 μm) and marine snow (> 500 μm) particles
56 (Simon et al., 2002) transport carbon from the surface into the deep ocean, is a key part of the global
57 carbon cycle (Neuer et al., 2014; Turner, 2015). Organic matter flux into the deep ocean (>1000 m) is a
58 function both of export from the photic zone into the mesopelagic (export flux), and the fraction of that
59 flux that crosses through the mesopelagic (transfer efficiency) (Francois et al., 2002; Passow & Carlson,
60 2012; Siegel et al., 2016). While definitions vary between studies, we define "mesopelagic" as the region
61 between the base of the photic zone, and 1000 m (following Francois et al., 2002; Cram et al., 2018). The
62 transfer efficiency of the biological pump may affect global atmospheric carbon levels (Kwon & Primeau,
63 2008). Thus, understanding the processes that shape organic matter degradation in the mesopelagic is
64 critical.

65 Oxygen concentrations, and especially the geographic and vertical extent of anoxic ocean regions, appear
66 to modulate particle flux through the mesopelagic. Observations of particle flux in the Eastern Tropical
67 North Pacific near the Mexican coast (Hartnett & Devol, 2003; Van Mooy et al., 2002; Weber & Bianchi,
68 2020), the Eastern Tropical South Pacific (Pavia et al., 2019), and Arabian Sea (Keil et al., 2016; Roullier
69 et al., 2014) have suggested lower flux attenuation in these ODZ systems. Models have shown that
70 accounting for oxygen limitation in ODZs is necessary to fit global patterns of particle transfer (Cram et
71 al., 2018; DeVries & Weber, 2017). Analysis of remineralization tracers has also shown evidence of slow
72 flux attention in the ODZs (Weber & Bianchi, 2020). Understanding the driving mechanisms of these
73 patterns is important because the oxygen content of the ocean is decreasing (Ito et al., 2017; Schmidtko et
74 al., 2017), and the spatial extent and depth range of ODZs, including the Eastern Tropical North Pacific
75 (ETNP) Oxygen Deficient Zone (ODZ), are likely to change, though there is disagreement over whether
76 they are expanding or undergoing natural fluctuation (Deutsch et al., 2014; Horak et al., 2016; Stramma et
77 al., 2008). Recent data informed models suggest that ODZs may enhance carbon transport to the deep
78 ocean, by inhibiting microbial degradation of sinking marine particles (Cram et al., 2018). However,
79 biological organic matter transport is also modulated by zooplankton whose interactions with particle flux
80 in pelagic ODZs are only beginning to be quantitatively explored (Kiko et al., 2020).

81 Zooplankton modulate carbon flux through the mesopelagic (Jackson & Burd, 2001; Steinberg & Landry,
82 2017; Turner, 2015), and by extension the transfer efficiency of the biological pump (Archibald et al.,
83 2019; Cavan et al., 2017), in three key ways that could be affected by ocean oxygen concentrations:

84 (1) *Active transport*: Zooplankton migrate between the surface and mesopelagic, consuming plankton and
85 particles in the surface and producing particulate organic carbon (POC), dissolved organic carbon (DOC),

86 respiratory CO_2, and zooplankton carcasses at depth (Archibald et al., 2019; Bianchi et al., 2013;

87 Hannides et al., 2009; Steinberg et al., 2000; Stukel et al., 2018, 2019). This manuscript focuses on

88 particles, so we only consider POC and carcass production, which cause particles to "appear" in the

89 midwater.

90 (2) *Repackaging*: Zooplankton fecal pellets have different physical properties than the parrticles and

91 plankton that they ingest (Wilson et al., 2008). In this paper we define repackaging as zooplankton

92 feeding in the mesopelagic and producing fecal pellets, effectively aggregating POM.

93 (3) *Disaggregation*: Zooplankton break large particles into smaller ones in two ways – by Coprorhexy

94 (also sometimes called sloppy feeding) in which they break particles apart while feeding on them

95 (Lampitt et al., 1990; Noji et al., 1991; Poulsen & Kiørboe, 2005), and by generating turbulence while

96 they swim (Dilling & Alldredge, 2000; Goldthwait et al., 2005). Disaggregation can reduce particle

97 transfer efficiency, because smaller particles sink more slowly and so reside longer in mesopelagic,

98 allowing them to be consumed before reaching deep waters (Goldthwait et al., 2005; Lampitt et al., 1990;

99 Noji et al., 1991; Poulsen & Kiørboe, 2005). In some cases, disaggregation can explain around 50% of the

100 particle flux attenuation over depth (Briggs et al., 2020).

101 The migratory zooplankton that drive these mesopelagic processes spend the night in the surface layer

102 and migrate into the core of the OMZ during the day (Bianchi et al., 2014).These organisms likely survive

103 in ODZs by slowing their metabolic processes, but may supplement these with very efficient oxygen

104 uptake and anaerobic metabolism (Seibel, 2011). Acoustic data suggest that zooplankton do not migrate

105 as deeply into ODZs as they do into regions where ODZs are absent (Bianchi et al. 2011). New evidence

106 suggests that in ODZ regions with shallower oxyclines, night-time migration depth remains the same but

107 the depth where the organisms spend the day is compressed (Wishner et al., 2020). The rates at which

108 zooplankton transport, repackage and disaggregate particles in ODZs are difficult to measure and

109 therefore poorly constrained. Despite the importance of zooplankton mediated processes to global carbon

110 flux, zooplankton are often missing from models of particle transfer.

111 Current models of particle transfer through the mesopelagic ocean predict that particle size, ocean

112 temperature, and oxygen concentrations are the dominant factors controlling particle flux attenuation

113 (Cram et al., 2018; DeVries & Weber, 2017). These models, however, do not account for active transport

114 or disaggregation by zooplankton. As a result of this assumption, the models predict that small particles

115 preferentially attenuate with depth, which is often not borne out by observations (Durkin et al., 2015).

116 Therefore, these models' predictions provide a useful null hypothesis of expected particle size

117 distributions in the absence of zooplankton effects, which can be compared to observed distributions of

118 particles to explore the magnitude of zooplankton effects.

4

119 Underwater vision profilers are cameras that can count and size many particles over large water volumes

120 (Picheral et al., 2010) and provide valuable information about particle distributions and transport. When

121 deployed in concert with particle traps in some regions, they can be used to predict flux in other regions

122 where traps have not been deployed (Guidi et al., 2008; Kiko et al., 2020). Connecting UVP and trap data

123 can furthermore inform about total particle flux variability across space and time, relationships between

124 particle size, biomass, composition, and sinking speed, as well as the contributions of the different

125 particle sizes to flux (Guidi et al., 2008; Kiko et al., 2017). Combined particle trap flux and UVP data

126 from the North Atlantic suggest active transport by zooplankton into hypoxic water (Kiko et al., 2020),

127 but the authors suggest that in more anoxic and larger ODZs, such as the modern day ETNP, there might

128 be reduced active transport into the mesopelagic, since many migratory organisms would presumably not

129 migrate into the anoxic water and would be less active. In this manuscript we provide the first combined

130 flux measurement and UVP data from such a fully anoxic region, the ETNP ODZ.

131 In addition to being fully anoxic, the ETNP ODZ is primarily oligotrophic: most of the volume of the

132 ETNP ODZ is below regions of very low surface productivity (Fuchsman et al., 2019; Pennington et al.,

133 2006). Meanwhile most flux data have been measured in more coastal, higher productivity regions of the

134 ETNP (Hartnett & Devol, 2003; Van Mooy et al., 2002).

135 A recent modeling study posed three hypotheses to explain why particle flux attenuates slowly in ODZs

136 (Weber & Bianchi, 2020), which are susceptible to testing with UVP data. These are: **H1:** *All* particles in

137 ODZs remineralize more slowly than in oxic water, regardless of their size, due to slower carbon

138 oxidation during denitrification than aerobic respiration. **H2:** Breakdown of large particles into small

139 particles is suppressed in the ODZ because there is less disaggregation by zooplankton than elsewhere.

140 **H3:** Large particles remineralize more slowly in ODZs, but smaller ones do not, because carbon oxidation

141 in large particles can become limited by the diffusive supply of oxygen and nitrate. In this case,

142 respiration can only proceed by thermodynamically inefficient sulfate reduction (Bianchi et al., 2018;

143 Lam & Kuypers, 2011). Sulfide and organic matter sulfurization have been found on particles at this site

144 at nanomolar concentrations (Raven et al., 2021). Microbial analysis of particles found sulfate reducers

145 and S-oxidizing denitrifiers at low abundances (Fuchsman et al., 2017; Saunders et al., 2019). Each of the

146 hypotheses outlined above were predicted to leave distinct signatures in particle size distributions in the

147 core of ODZ regions (Weber & Bianchi, 2020). The model with slow remineralization of all particles,

148 predicts an increase in the abundance of small particles in the ODZ core relative both to overlying waters

149 and to similar, oxygenated environments (**H1**). The model with suppressed disaggregation predicts a large

150 decrease in small particle biomass in the ODZ, both relative to the surface and to oxygenated water (**H2**).

151 The model in which remineralization is depressed only in large particles predicts a small decrease with

5

depth in small particle abundance, similar to that seen in oxygenated environments (**H3**). However, the necessary particle size data from an ODZ was not previously available to support any hypothesis at the exclusion of the others. In this manuscript we present a new dataset that is sufficient to test these three hypotheses.

To provide the data to test hypotheses **H1-H3** and illuminate zooplankton particle interactions in oligotrophic ODZs, we collected particle size data at high temporal resolution over the course of a week in an anoxic site typical of the oligotrophic ETNP ODZ, well away from the high productivity zone in the coast. We integrated this size data with observed flux measurements, and acoustic data. We quantified, throughout the water column, how changes in size distribution deviate from changes that would be predicted by remineralization and sinking only models.

We ask the following four questions:

Question A: How does the particle size distribution at one location in the oligotrophic Eastern Tropical North Pacific vary with respect to depth and time?

Question B: Do our data support any of the three Weber and Bianchi (2020) models (**H1-H3**)?

Question C: Do our data suggest that regions of the oxygen deficient zone harbor disaggregation-like processes, and if so, do these co-occur with migratory zooplankton?

Question D: How do particle size distribution spectra in the ODZ compare to those seen in the oxic ocean?

By addressing these four questions, we demonstrate that our dataset from the ETNP supports Weber and Bianchi's first hypothesis, that microbial remineralization of all particles slows in the ODZ, while disaggregation continues unabated. Additionally, disaggregation-like processes do appear to co-occur with acoustic measurements of migratory zooplankton, suggesting that exclusion of zooplankton is not a major contributor to slow flux attenuation.

5 Methods

Unless specified otherwise, measurements were taken on board the R/V *Sikuliaq*, cruise number SKQ201617S, from 07 January 2017 through 13 January 2017 at a single station 16.5°N 106.9°W, which was located in an oligotrophic region of the Eastern Tropical North Pacific Oxygen Deficient Zone (ETNP Station P2; Figure 1A). Data are compared against measurements taken at 16.5°N 152.0°W on 08 May 2015, collected on the GO-SHIP CLIVAR/CARBON P16N Leg 1 Cruise (CCHDO Hydrographic Cruise 33RO20150410). This station was at the same latitude as ETNP Station P2, west of the ODZ, but was not anoxic (P16 Transect Station 100; Figure S1).

6

5.1 Water property measurements

We measured water properties of temperature, salinity, fluorescence, oxygen concentration and turbidity using the shipboard SeaBird 911 CTD. Auxiliary sensors included a WetLabs C-Star (beam attenuation and transmission) and a Seapoint fluorometer. Data were processed with Seabird Software, (programs– data conversion, align, thermal mass, derive, bin average and bottle summary) using factory supplied calibrations. Data was analyzed and visualized in *R* (Team 2011). Processed data are available under NCEI Accession number 1064968 (Rocap et al., 2017).

5.2 Water mass analysis

Evans et al. (2020) previously employed optimum multiparameter analysis to map the percent identity of the water observed at each depth to three water masses: the 13 Degree Celsius Water (13CW), North Equatorial Pacific Intermediate Water (NEPIW), and Antarctic Intermediate Water (AAIW). We subset and examine only the portion of these data that correspond to our site.

5.3 Acoustic Measurements

Backscattering signals from the ship-board EK-60 were collected and archived by UNOLS as raw data files. We used Echopype software (Lee et al., 2021) to convert these raw files to netcdf files, which were down-sampled to five minute time-step resolution, saved as a text file, and later visualized in R. The acoustic data appeared to be off by one hour and so one hour was subtracted from all time measurements. This correction resulted in zooplankton vertical migrations being synchronized with the diel light cycle as was recorded on board the ship by JAC.

5.4 Particle size measurements

Particle size data were collected by an Underwater Vision Profiler 5 (UVP) that was mounted below the CTD-rosette and deployed for all CTD casts shallower than 2500 m. A UVP is a combination camera and light source that quantifies the abundance and size of particles from 100 μm to several centimeters in size (Picheral et al., 2010). UVP data were processed using the Zooprocess software, which prepares the data for upload to the Ecotaxa database (Picheral et al., 2017); data from all UVP instruments are located on this online database for ease of access. Detailed descriptions for installation of the Zooprocess software can be found on the PIQv website (https://sites.google.com/view/piqv/zooprocess-uvpapp). Zooprocess uses the first and last image number selected by the user in metadata to isolate the downcast and process this subset for both particle size distribution and image data. The processed files and metadata are then uploaded to a shared FTP database where it is available for upload to Ecotaxa. This project required the extra step of filtering out images due to the discovery of an issue with the lighting system, where only one of the two LEDs would illuminate, resulting in an incomplete sample. The filtering procedure is

7

215 documented in a link available at the same location as the Zooprocess download. Images where only a

216 single light illuminated were removed from the dataset before it was uploaded on to Ecotaxa. Once

217 uploaded to Ecotaxa, data were downloaded from EcoPart (the particle section of the database) in detailed

218 TSV format, and analyzed in R. The UVP provided estimates of abundances of particles in different size-

219 bins, as well as information about the volumes over which those particle numbers had been calculated.

220 The instrument is capable of observing smaller particles (down to 60 μm), but these tend to be

221 underestimated and so are excluded from the analysis. The instrument can in principle also measure larger

222 particles (up to the field of view of the camera), though these tend to be scarce enough to be not detected.

223 In this paper, we do not have an upper size cut-off for our analysis and rather implement statistics that are

224 robust to non-detection of scarce large particles (section 5.5.1). Visual inspection of images larger than

225 1 mm suggests that these large particles are primarily "marine snow" but about 5% are zooplankton. We

226 did not quantify the size distribution of these images.

5.5 Flux measurements

228 Free floating, surface tethered particle traps were used to quantify carbon fluxes from sinking particles.

229 Arrays, consisting of a surface float and two traps, were deployed and allowed to float freely during

230 which time they collected particles. Trap deployments began on 07 January, concurrently with the

231 beginning of the UVP sampling, and continued through 12 January. Trap recovery began on 08 January

232 and continued through 13 January. Trap depths spanned the photic zone and mesopelagic, with the

233 shallowest at 60 m and the deepest at 965 m. Trap deployments lasted between 21 and 91 hours, with

234 deeper traps left out for longer, to collect more biomass. Two types of traps were deployed. One set of

235 traps, generally deployed in shallower water, had a solid cone opening with area 0.46 m^2. The second set

236 had larger conical net with opening of 1.24 m^2 area made of 53 μm nylon mesh similar to the description

237 in Peterson et al. (2005). All equipment were combination incubators and particle traps, but in this study

238 we only use trap data. No poisons were used, and both living and dead zooplankton, or 'swimmers', were

239 manually removed prior to POC analysis.

240 Sediment trap material was filtered immediately upon trap recovery onto pre-combusted GF-75 45 mm

241 filters (nominal pore size of 0.3 μm) and preserved until further analysis at -80°C. These filters were split

242 into several fractions for other analyses not discussed here. Total carbon content of particles in each trap

243 were measured by isotope ratio mass spectrometry. Elemental analyses for particulate carbon and nitrogen

244 quantities as well as ^{13}C and ^{15}N isotopic compositions were conducted at the U.C. Davis Stable Isotope

245 Facility (http://stableisotopefacility.ucdavis.edu) on acidified freeze-dried trap samples to capture organic

246 elemental contributions. Carbon was below mass spectrometry detection limits in four traps – these traps

247 were excluded from further analysis. Traps at similar depths did detect carbon, lending confidence to the

248   idea that these non-detections were technical in nature, due to splitting of samples for multiple analyses,

249   rather than reflecting environmental conditions.

5.6   Analysis

251   Particles were binned by depth with 20 m resolution between the surface and 100 m, 25 m resolution

252   between 100 m and 200 m depths and 50 m resolution below 200 m. This increasing coarseness of the

253   depth bins helped account for more scarce particles deeper in the water column, while maintaining higher

254   depth resolution near the surface. To perform this binning, particle numbers, and volumes of water

255   sampled of all observations within each depth bin were summed prior to other analyses. Most analyses

256   focused on the mesopelagic, defined here as the region between the base of the secondary chlorophyll

257   maximum layer (160 m — hereafter the base of the photic zone), which is within the ODZ, and 1000 m.

258   Two normalized values of particle numbers were calculated. In the first, particle numbers were divided by

259   volume sampled, to generate values in *particles/m³*. In the second, particles were divided by both volume

260   sampled and the width of the particle size-bins to generate values in *particles/m³/mm*.

5.6.1   Particle size distribution

262   We determined the slope and intercept of the particle size distribution spectrum by fitting a power law to

263   the data, which is a common function for fitting particle size distributions (Buonassissi & Dierssen,

264   2010). Because large particles were infrequently detected, we used a general linear model that assumed

265   residuals of the data followed a negative-binomial (rather than normal) distribution. We fit the equation

266     $\ln\left(\frac{E(Total\ Particles)}{Volume*Binsize}\right) = b_0 + b_1\ ln(Size)$ (Eqn 1).

267   to solve for the Intercept (b_0) and particle size distribution slope (PSD $= b_1$). On the left-hand side of

268   Eqn 1. *E(Total Particles)* refers to the expected number of particles in a given depth and particle size bin

269   assuming a negative binomial distribution of residuals (Date, 2020; Ooi, 2013). *Volume* indicates the

270   volume of water sampled by the UVP, or in the case of depth-binned data, the sum of the volumes of all

271   UVP images in that depth interval. *Binsize* indicates the width of the particle-size bin captured by the

272   UVP. Thus, if particles between 0.1 and 0.12 mm are in a particle size bin, the *Binsize* is 0.02 mm. On the

273   right-hand side of Eqn 1, *Size* corresponds to the lower bound of the particle size-bin. We use the lower

274   bound of a particle size-bin, rather than its midpoint, because, due to the power-law particle size

275   distribution slopes, the average size of particles in each size-bin is closer to the size-bin's lower bound

276   rather than its midpoint.

5.6.2 Estimating particle flux

We estimated particle flux throughout the water column, by fitting particle data to trap measurements. We assumed that particle flux in each size bin (j) followed the equation

$$\text{Flux} = \sum_j \left[\frac{Total\ Particles_j}{Volume * Binsize_i} * C_f * (Size_j)^A \right] \qquad \text{(Eqn. 2)}$$

Such that flux at a given depth is the sum of all size-bin specific values.

We used the *optimize()* function in *R*'s stats package to identify values for the C_f and A coefficients in Eqn 2. that yielded closest fits of the UVP estimated flux to each particle trap.

We also estimated the exponent of the particle size to biomass exponent α and size to sinking speed exponent γ per the equations $\text{Biomass}_j \sim \text{Size}_j^\alpha$ and $\text{Speed}_j \sim \text{Size}_j^\gamma$. This is done by assuming a spherical drag profile, in which case $A = \alpha + \gamma$ and $\gamma = \alpha - 1$ (Guidi et al., 2008); with "A" referring to the exponent in Eqn 2.

5.6.3 Size specific information

We separately analyzed total particle numbers, particle size distribution, and particle flux for particles larger than or equal to 500 μm, and those smaller than 500 μm, to determine the relative contributions of these two particle classes to particle properties. 500 μm was chosen as it has been previously defined as the cutoff point between microscopic "microaggregates" and macroscopic "marine snow" (Simon et al., 2002).

5.7 Variability

To explore the timescales of temporal variability in the POC flux, we determined how well the flux at each depth horizon can be described by the sum of daily and hourly temporal modes. This was achieved by fitting the general additive model of form

$$\text{Flux}^{1/5} \sim s(\text{Depth}) + s(\text{Day}) + s(\text{Hour}) \qquad \text{(Eqn. 3)}$$

This model explored whether estimated flux levels appeared to vary by decimal day and decimal hour, holding the effects of depth constant, in the 250 m to 500 m region. The smooth terms *s* for *Depth* and *Day* were thin plate splines, while the *s* term for *Hour* was a cyclic spline of 24-hour period.

5.8 Smoothing for Comparison to Model Results

Normalized particle abundance data, from the only UVP cast that traversed the top 2000 m of the water column, taken on January 13 at 06:13, was smoothed with respect to depth, time, and particle size using a general additive model of the form

10

306 $\quad \ln\left(\frac{E(Total\ Particles)}{Volume*Binsize}\right) \sim s\big(\text{Depth, } \ln(\text{Size})\big) \qquad \text{(Eqn. 4)}$

307 In this case, there is a single, two-dimensional, smooth term, rather than additive one-dimensional terms

308 as in Eqn. 3 so that the smooth term can consider interactions between the two parameters, rather than

309 assuming that the terms are additive. The predicted particle numbers at each particle size and depth, as

310 well as particle size distribution spectra, and estimated particle masses of all particles smaller than

311 500 μm and all particles larger than or equal to 500 μm were then compared to each of Weber and

312 Bianchi's (2020) models, corresponding to our **H1-H3**.

5.9   Modeling remineralization and sinking

314 To quantify disaggregation, our goal was to compare the particle size-abundance spectrum at each depth

315 to a prediction of the null hypothesis, that it is simply governed by the effects of sinking and

316 remineralization reshaping the spectrum observed shallower in the water column. This prediction is

317 generated using the particle remineralization and sinking model (PRiSM), modified from DeVries et al.

318 (2014), which we applied to the shallower spectrum as an initial condition. The difference between the

319 null hypotheses prediction and observation indicates the role of processes not accounted for in PRiSM,

320 such as disaggregation, aggregation, and active or advective transport of particles with a different size

321 spectrum than the ones seen at the deeper depth.

322 In practice we expanded the previous numerical implementation of PRiSM to allow for particle size

323 distribution spectra with particle-size bins that match those obtained by the UVP, and to return estimates

324 of the number of particles in those same size bins (Text S1). The model accepts inputs of particle size

325 distributions at each depth, and changes in particle flux between each depth-bin and the next, deeper,

326 depth-bin. The model optimizes a particle remineralization rate that would result in that observed flux

327 loss. It finally returns a "predicted" particle size distribution spectrum that has total flux equal to the flux

328 of the observed deeper spectrum that would be expected if the shallower spectrum only sank and

329 remineralized. In cases where flux increased with depth, particles are assumed to put on mass rather than

330 lose mass following a negative remineralization rate. Here, "negative remineralization" stands in for

331 chemoautotrophy, active transport, and other processes that result in flux increases with depth. While

332 these processes likely have more complex effect on the particle size distribution than is accounted for in

333 our model, we note that flux increases with depth are very rare, and that allowing for negative

334 remineralization allows our null model to be robust in those rare cases.

11

6 Results

6.1 Physical and Chemical Data

The ODZ, characterized in this study by oxygen levels less than 1 µM, as measured by the CTD, extends from 90 m to 900 m depth, with a sharp upper oxycline and a gradual lower oxycline (Figure 1B-C). This station has been previously proven to be anoxic with a STOX sensor (Tiano et al., 2014). The upper oxycline tracks a sharp pycnocline (Figure 1B-1D), set by the high salinity of the 13CW water mass (Figure S2), and is characterized by an abrupt drop in temperature below the mixed layer and an increase in salinity (Figure 1B). Water mass analysis indicated that water in the top part of the ODZ is dominated by the 13CW water mass, while water between 275 and 500 m is primarily from the NEPIW, with water from the AAIW dominating in the lower 500 m (Figure S2) (Evans et al., 2020). The site is characterized by two fluorescence maxima (Figure 1C). The larger, shallower fluorescence peak is positioned just above the oxycline, with fluorescence from this peak and oxygen attenuating together. The smaller, lower peak is inside of the ODZ. Turbidity tracks the two chlorophyll peaks in the surface and has a tertiary maximum at the lower oxycline (Figure 1D). The cyanobacteria at the secondary chlorophyll maximum are known to be photosynthesizing and producing organic matter in the ODZ (Fuchsman et al., 2019; Garcia-Robledo et al., 2017). To avoid complication due to this source of organic matter production, we focus our further analysis below 160 m.

For the purposes of this study, we define the photic zone as ending at the base of this deeper fluorescence layer (160m). This photic zone base corresponds with photosynthetically active radiation (PAR) $< 10^{-5}$ of surface PAR levels (Figure 1C). We note that this photic zone depth is deeper than conventional definitions, in which the base of the photic zone corresponds with 10^{-2} (90 m) or 10^{-3} (120 m) of surface PAR.
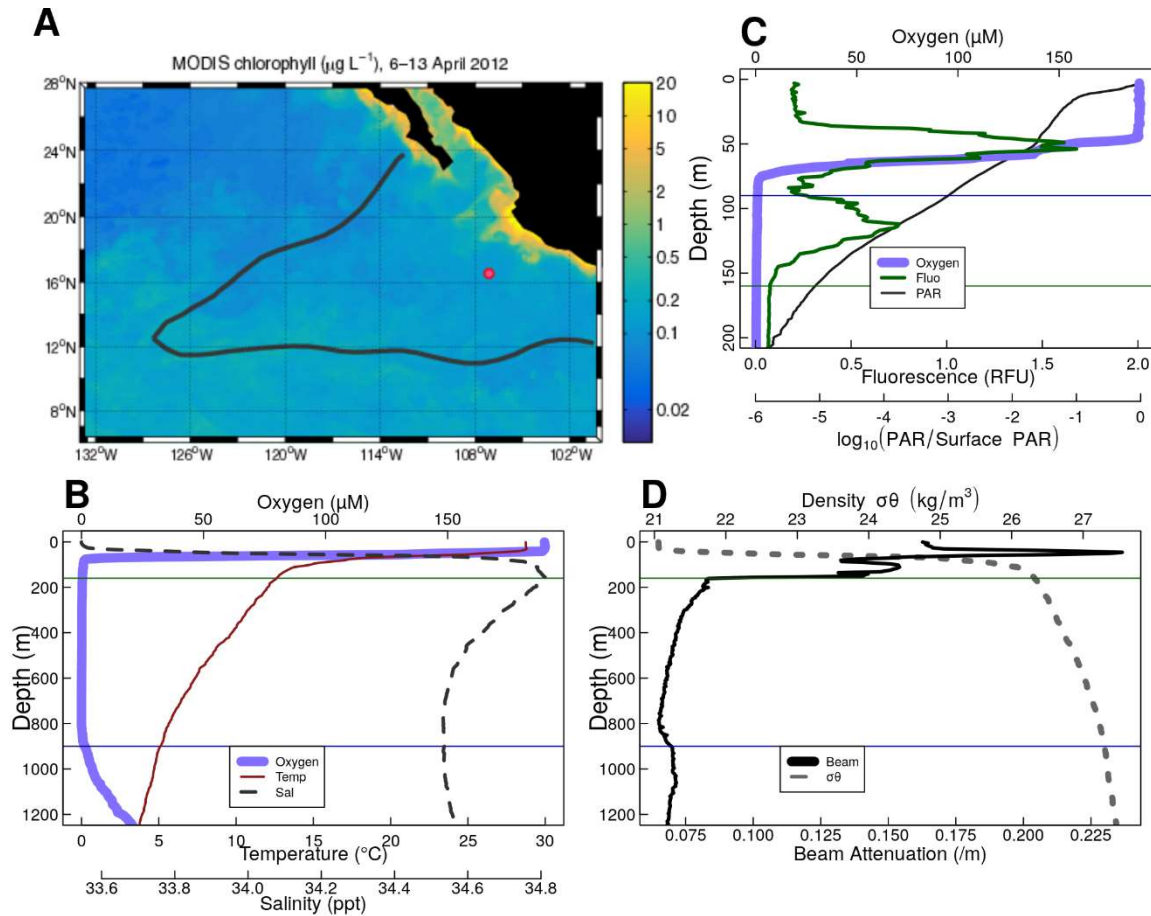
12

Figure 1. Overview of the geography, physics, and chemistry of ETNP Station P2. **A.** Map of the ETNP Oxygen Deficient Zone and the location of Station P2. Colors indicate chlorophyll concentrations at the surface as determined by MODIS satellite in 2012, while the black outline signifies the region containing <10 μM oxygen at 300 m, according to World Ocean Atlas. The red circle indicates the location of Station P2 (modified from Fuchsman et al 2019, credit Hilary Palevsky, Creative Comments License https://creativecommons.org/licenses/by/4.0/). **B-D.** Oceanographic parameters collected from a cast at 2017-01-13 12:15 CST (local time). The thin horizontal green line shows the location of the base of the photic zone (160 m B-D), defined by the complete attenuation of the in-situ fluorescence, while the horizontal blue lines show the surface (90 m, C) and base of the ODZ (900 m, B,D). **B.** shows temperature, salinity and oxygen. **C.** fluorescence and photosynthetically available radiation (PAR), focusing on the top 200 m of the water column and photosynthetically active radiation, and **D.** beam attenuation and density.

6.2 Acoustic data reveal diel migration patterns

Acoustic data, produced by the shipboard EK60 (Andersen, 2001), at ETNP Station P2, suggest the presence of multiple cohorts of migratory organisms. We focus initially on backscattering measurements from the EK60's lowest frequency 18000 Hz signal, corresponding to organisms the size of small fish, because it travels furthest into the water column and has the best resolution of the channels. Most migratory organisms appeared to leave the surface at dawn and return at dusk, spending the day between 250 m and 500 m (Figure 2A). There appeared to be two local maxima in backscattering intensity at mid-day, one at ~300 m and one at ~375 m (Figure 2A). There also appeared to be organisms that reverse migrated downward at dusk and upward at dawn, spending the night at ~300 m (Figure 2B). Just above the base of the photic zone, there was a peak of organisms that appeared, at mid-day, on some but not all days, without any visible dawn or dusk migration. (Figure 2C). Some diel migrators appeared to cross the ODZ and spend the day below the detection range of the EK60 (Figure 2D), as well as organisms that appeared between 500 m and 1000 m but did not appear to migrate to or from that depth at our site, but rather traveled through the EK60's field of view (Figure 2E). Similar patterns were evident in each of the other measured frequencies, with better resolution by the lower frequencies (Figure S3).
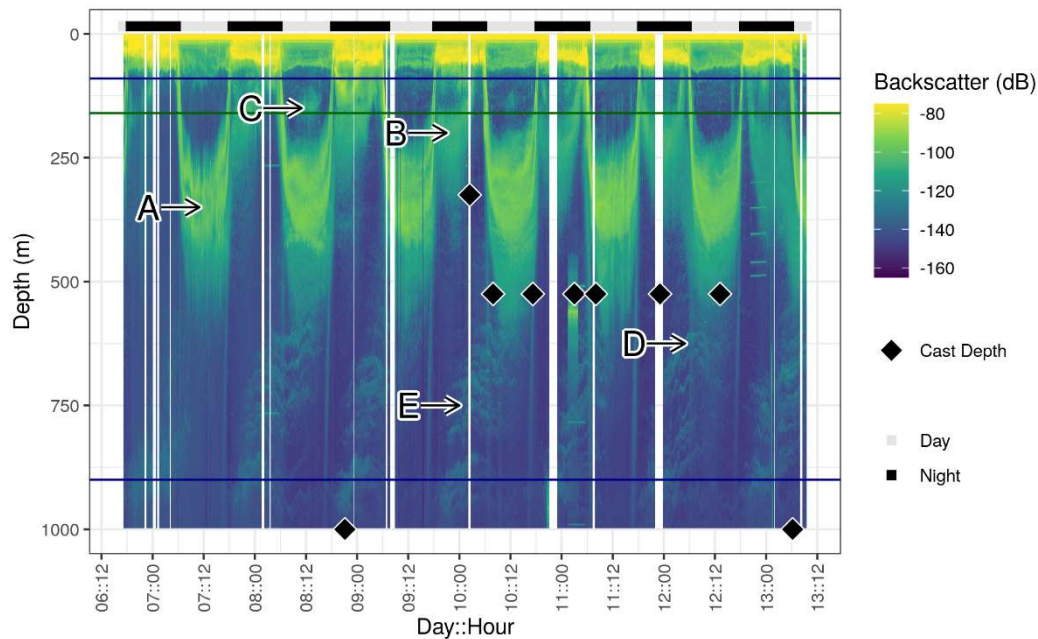

Figure 2. Acoustic data, measured by EK60 over the course of the experiment, at ETNP Station P2. Shown are data from the 18000 Hz frequency band, which have highest depth penetration, but which appear to co-occur with data from other frequency bands (see Figure S3). Values are in return signal intensity and have not been normalized to observed biomass. Horizontal blue lines indicate the top and bottom of the ODZ, while the horizontal green line indicates the base

14

of the photic zone. Times are local Mexico General Standard time, which is the local time for the nearest port of call in Manzanillo and is equivalent to United States Central Standard Time. The black and white bar at the top indicates day and night periods, with day defined as times when the center of the sun is above the horizon, per the OCE R package. Diamonds indicate the depths and times of UVP casts, with casts deeper than 1000 m shown as diamonds on the 1000 m line. Several patterns are evident **A.** Two bands of organisms can be seen leaving the surface at dawn, spending the day between 250 m and 500 m and returning to the surface at dusk. **B.** Another group of nocturnally migrating organisms can be seen leaving the surface at dusk, spending the night near 250 m and returning at dawn. **C.** Some organisms appear at the base of the photic zone, during some, but not all mid days, and then disappear in the evening. **D.** A group of very deep migrating organisms appears to leave the surface with the diel migrators and pass all the way through the ODZ and out of the EK60's field of view. It returns at dusk. **E.** Swarms of organisms appear between 500 m and 1000 m disappearing later in the day. Swarms appear in the deepest layers at night and appear progressively shallower as the day progresses.

6.3   Flux data from traps

Flux measurements at Station P2 were consistent between the different particle trap types, showing a profile that broadly followed a power law with respect to depth, with the exception that flux appeared to increase in one trap at 500 m (Figure 3).
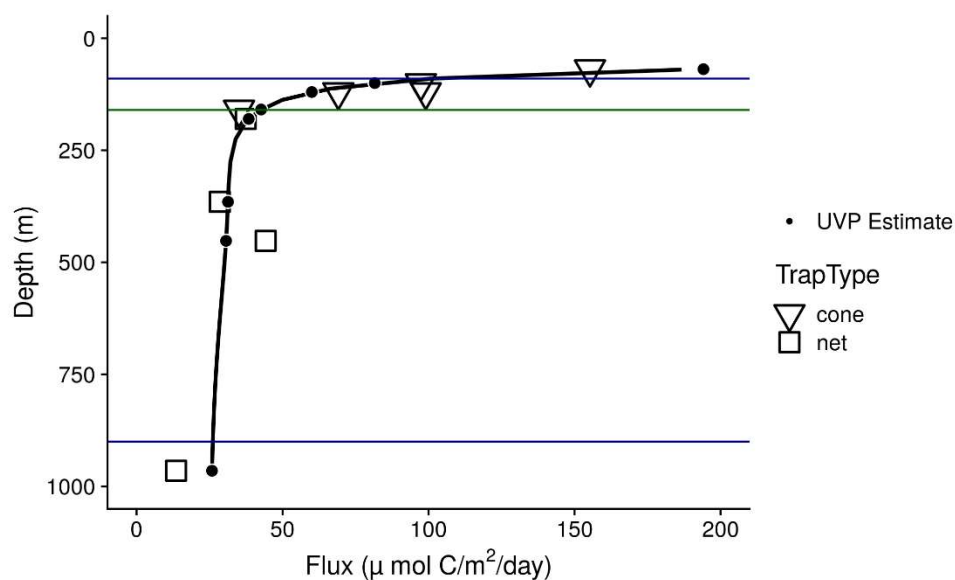

Figure 3. Sinking particle flux, measured from surface-tethered sediment traps (large symbols), at ETNP Station P2. Trap types are shown by the shape of the large points. Superimposed are

15

414   estimates of particle flux from the UVP generated by fitting the sum of particle numbers all four

415   profiles to the trap observed flux. The black line indicates flux predictions made by fitting UVP

416   observations to the trap data. Black circles indicate regions on the black line corresponding to

417   the trap observation depths. Horizontal blue lines indicate the top and bottom of the ODZ, while

418   the horizontal green line indicates the base of the photic zone.

6.4   Particle abundance measurements vary with size and depth

420   In all profiles, particle abundances were highest at the surface, and highest among the smallest particles

421   (Figure S4). Visual examination of the relationship between particle number and size suggested a power

422   law relationship where the log of volume and bin-size normalized particle abundance was proportional to

423   the log of the particles' size (Figure S5). The exception to this pattern were particles larger than 10 mm

424   (Figure S4, S5), which are rare enough that they are usually not detected by the UVP. Generalized linear

425   models that assume a negative-binomial distribution of the data accounted for this under-sampling of

426   large particles to estimate power law slopes, while considering rare occurrences of the large particles at

427   each depth (Figure S5).

428   Total particle numbers were generally similar between different casts, regardless of which day or hour

429   they were collected (Figure 4A). Particle numbers were highest in the surface and decreased within the

430   oxic region, then remained relatively constant from 160 m to 500 m, and gradually decreased between

431   500 m and the lower oxycline (Figure 4A).

432   The particle size distribution slope generally steepened (became more negative) between the base of the

433   photic zone (160 m) and 500 m, flattened (became less negative) between 500 m and 1000 m, and then

434   steepened again below 1000 m (Figure 4B). Steeper, more negative, slopes indicate a higher proportion of

435   small particles relative to large particles, while flatter, less negative, slopes indicate a more even particle

436   size distribution. Flatter distributions still have a higher *absolute number* of smaller particles than larger

437   particles; however, they have a higher *proportion* of larger particles relative to other samples with steeper
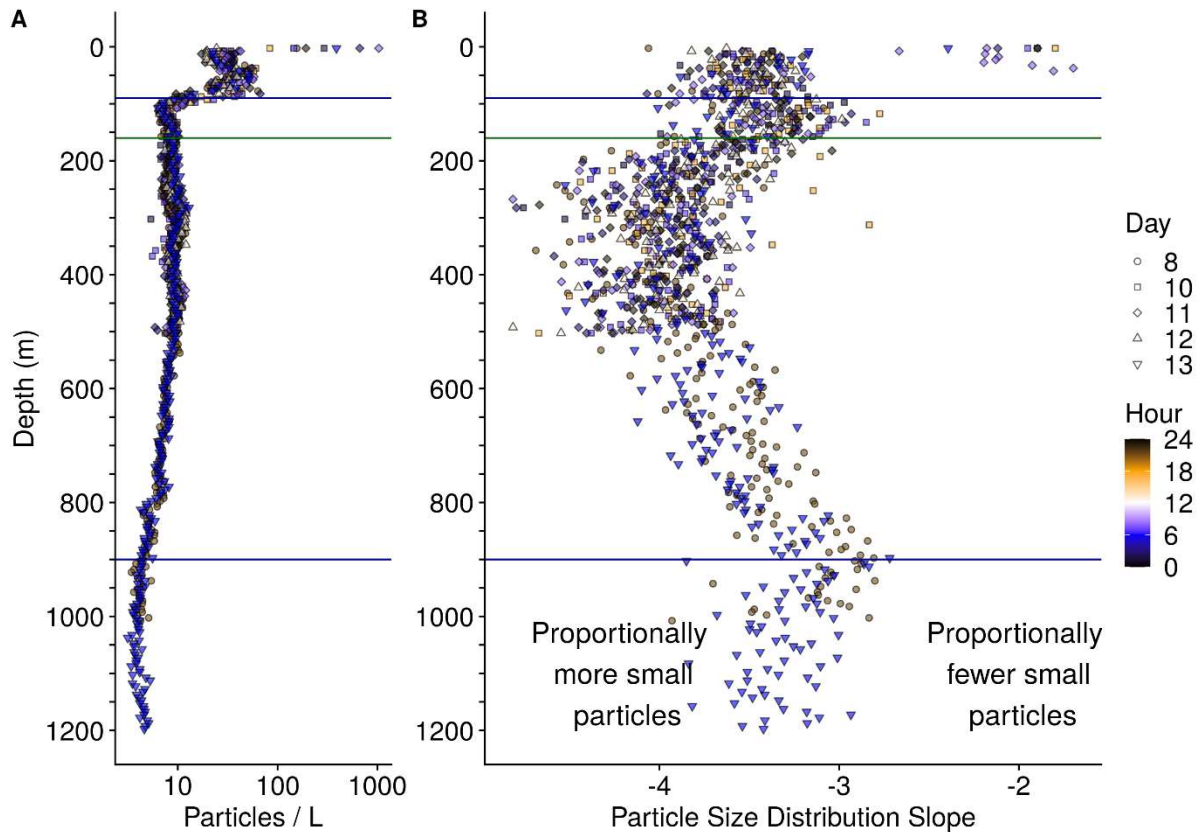
438   distributions.

16

Figure 4. A. Observed, volume normalized total particle numbers from 9 casts taken at different times of the day at ETNP station P2. **B.** Calculated particle size distribution slopes of those particles. These data have not been binned by depth in order to better show sample to sample variability. Horizontal blue lines indicate the top and bottom of the ODZ, while the horizontal green line indicates the base of the photic zone. Hour corresponds to local, Mexican General Standard, time.

6.5 Estimated particle flux sometimes increases with depth in the ODZ core

Optimization found best agreement between particle flux measured by traps, and UVP estimated particle flux when per particle flux is fit by the equation

Flux = (133 μ mol C / m^2/day) = **133** * Size (mm) ^ **2.00**   (Eqn 5)

This equation represents an empirical relationship between particle flux from traps and particle size measured by UVP. Applying this fit to the UVP data resulted in a UVP predicted flux profile that broadly fit the expected trap observed flux profiles (Figure 3).

Particle flux profiles, predicted from the above particle size abundances and fit, varied between casts between the base of the photic zone and 500 m (Figure 5A-5B). To examine the rate of change of flux and

17

455   to identify regions and time points where flux appeared to increase with depth, we examined the rate of

456   change of flux. This rate of change was fifth root transformed to normalize the data and to allow us to

457   focus on the cases where flux attenuation varied about zero, since we were interested in identifying

458   factors that related to whether flux was positive or negative. Between 250 m and 500 m, particle flux

459   appeared to increase on some, but not all, casts, while attenuating slowly on the other casts (Figure 5C).

460   Below 500 m, there were not enough casts to measure variability between casts.

461   The general additive model that quantified how the of change of flux between 250 m and 500 m varied

462   with depth, decimal study day and decimal hour found that depth ($p = 0.061$) and hour of the day ($p =$

463   0.196) did not statistically associate with the fifth root transformed rate of change of flux while day of

464   study did ($p = 0.019$, $R^2 = 0.264$, Figure S6). There were generally increases in flux over this region

465   towards the beginning and end of the sampling period and decreases in flux nearer to day 10 (Figure

466   S6B). A general additive model that looked only at the relationship between study day and rate of change

467   of flux (fifth root transformed) in this region suggested that day accounted for 14% of the variance in this

468   value, as determined by adjusted R^2 ($p = 0.040$). If the fifth root transformation was not applied to the rate

469   of change of flux, there was a statistically significant relationship between depth and rate of change (p =

470   0.001), but not study day ($p = 0.062$) or hour ($p = 0.719$, $R^2 = 0.341$). This pattern indicated that, without

471   the transformation, any temporal signal is swamped by the substantial changes in rate of change in depth,

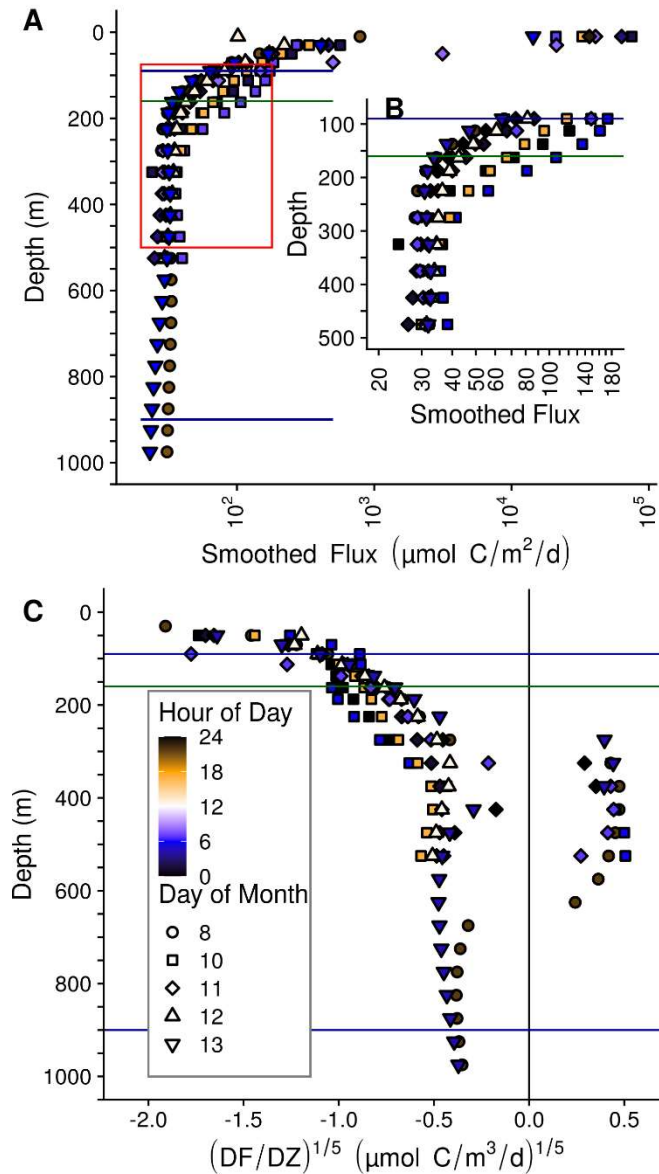472   with shallower depths losing flux faster than deeper ones.

18

Figure 5. Within and between day variability in UVP predicted particle flux at ETNP Station P2. All profiles are depth binned with higher resolution towards the surface (methods). Horizontal blue lines indicate the top and bottom of the ODZ, while the horizontal green line indicates the base of the photic zone. **A.** Flux profiles in the top 1000 m of the water column. **B.** A more detailed depiction of the area enclosed by the rectangle in **A**. -- **C.** The rate of change of flux, divided by the rate in change in depth. The fifth root of these values are shown to highlight differences between values close to zero. Hour corresponds to local, Mexican General Standard, time.

19

6.6 Smoothed and averaged data

At the ETNP ODZ site, highly smoothed particle abundance data suggested that particle size, averaged across all casts, followed a pattern in which the abundance of <500 μm particles increased between the oxycline and 350 m (Figure 6A), which corresponded with steepening of the particle size distribution slope (Figure 6B), and an increase in microaggregate (<500 μm) particle biomass (Figure 6C), but not of > 500 μm particle biomass (Figure 6D). Deeper in the ODZ, the microaggregate (<500 μm) particle number and biomass, and the particle size distribution slope declined.
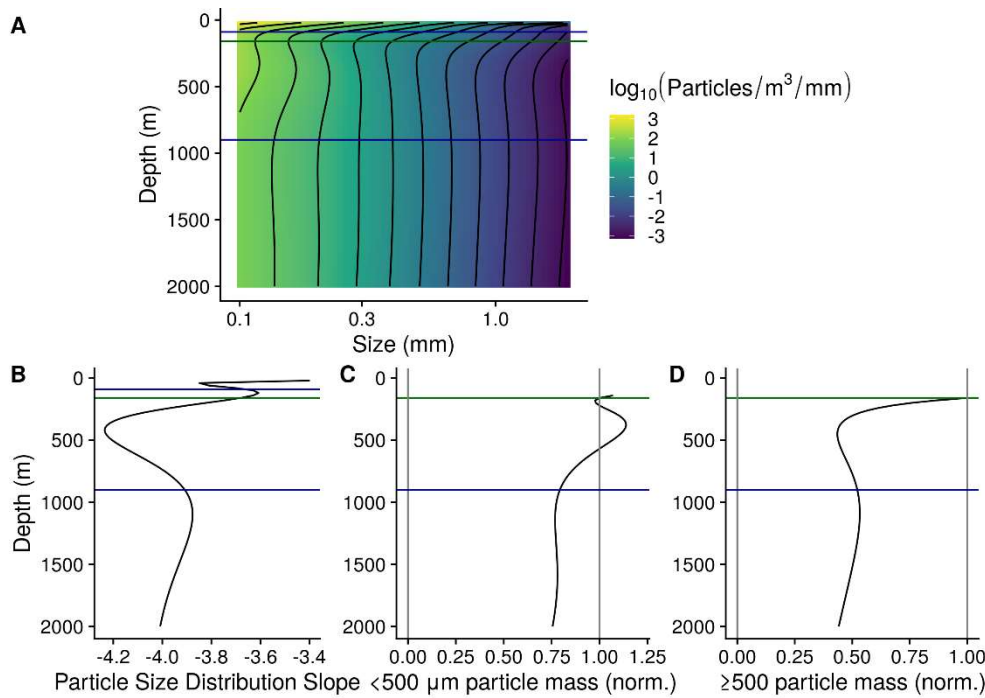
Figure 6. A. GAM smoothed, bin-size and volume normalized particle numbers across the particle size spectrum, at ETNP Station P2. Data are from the only cast that traversed the top 2000 m of the water column, collected on January 13 beginning at 06:13. Horizontal blue lines indicate the top and bottom of the ODZ, while the horizontal green line indicates the base of the photic zone. **B.** Particle size distribution slope. **C-D**. Estimated biomass of **(C)** microaggregate (<500 um) and **(D)** marine snow (≥500 um) particles, normalized to biomass at the base of the photic zone. In these two biomass panels, data from above the base of the photic zone are not shown.

At the oxic site, particle size distributions generally steepened with depth, while both microaggregates (<500 μm) and ≥500 μm estimated particle biomass followed a power law decrease with depth (Figure S10).

20

6.7 Particle number dynamics differ from model expectations

The modified particle remineralization and sinking model predicted particle size distributions at each depth from the particle size distribution one depth-bin shallower and the calculated flux attenuation between the two depths. At the ETNP ODZ site, we found that the observed particle size distributions usually deviated from model expectations (Figure S11). In the model, remineralization rates are optimized, to ensure that the total predicted flux at each depth matches the observed total flux. However, the predicted size spectrum will diverge from the observed spectrum if the assumptions of the model (i.e., sinking and remineralization are the only particle transformations) are violated. The difference between the observed and predicted flux of *microaggregate particles* (100 - 500 μm), normalized to depth, therefore serves as a metric of observed deviations from the size distribution expected from sinking and remineralization alone. We call this value *Deviation from Model* (DFM).

$$\text{DFM} = \frac{(<500 \, \mu m \, Flux \, Observed - \, <500 \, \mu m \, Flux \, Modeled)}{\Delta Z} \qquad \text{(Eqn. 6)}$$

In the above equation ΔZ is the distance, in meters, between the current depth bin and the previous depth bin, whose particle size distribution is fed into the predictive model.

DFM was positive between the base of the photic zone (160 m) and 500 m, meaning that less <500 μm particle flux attenuated than would be expected from the *PRiSM* model in this region (Figure 7). There was some variability in the DFM parameter between casts. A general additive model (GAM) that showed that the variability in DFM was statistically significantly related to depth ($p < 10^{-5}$), day of the study ($p = 0.002$), but not to hour of the day ($p = 0.051$), with these factors together explaining 41.6% of the variance, as measured by R^2. DFM was highest shallower in the water column (Figure S12A), highest near day 10 and lower at the beginning and end of the study (Figure S12B). A GAM that only explored the effect of depth accounted for 27.4% of the variance. Comparing a GAM that accounted for study day and depth to one that only accounted for depth effects showed an increase in R^2 value of 10.4%, suggesting that study day accounts for an additional 10.4% of the variance, after accounting for depth. Comparing the model that accounts for depth, day and hour to one that only accounts for depth and day, suggests that hour of the day, while not statistically significant, could explain an additional 3.4% of the variance. Below 500 m, DFM was negative. There were only two casts that reached below 500 m at this station, and so an analysis of the dynamics of DFM in this region is not possible. At P16 Station 100, DFM was positive between the base of the photic zone and 350 m and negative below 350 m (Figure S9C).
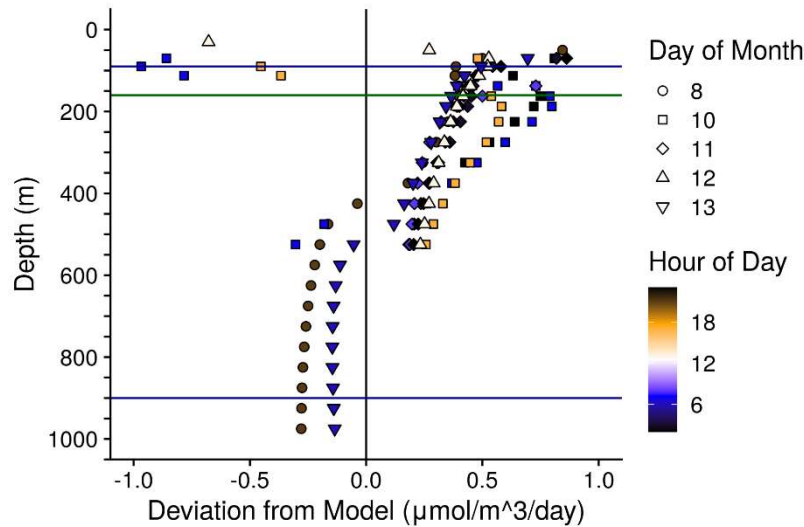
21

Figure 7. *Deviation from Model (DFM)* indicates the difference between the observed flux of small particles (< 500 μm), and the flux of small particles that would be estimated by a model, which assumes that particles in the depth bin above only remineralized and sank, following the PRiSM model. Values are normalized to the change in depth and are in units of μ mol Carbon $m^{-3}d^{-1}$. This value serves as a metric of processes that cannot be captured by a null model, which assumes that particles only sink and remineralize. Positive values suggest an excess of <500 μm particles, suggesting disaggregation or advection of small particles, while negative values suggest a dearth of small particles, suggesting repackaging or aggregation. DFM is only reported for <500 μm particles (<500 μm), because it is the inverse of the deviation from expected flux of ≥500 μm particles. *DFM* is reported for all casts at ETNP Station P2. Horizontal blue lines indicate the top and bottom of the ODZ, while the horizontal green line indicates the base of the photic zone.

6.8 ETNP particle dynamics differ from those seen at an oxic site

The ODZ data were compared to an oxic water column in order to identify the spectral signatures that are particular to oxygen deficient waters. The oxic site, P16 Station 100, was characterized by a more gradually sloping pycnocline, and an oxygen minimum at 500 m of 19.7 μM, which is hypoxic (Figure S1B). There was no working fluorescence sensor on that cruise, but data from World Ocean Atlas (Boyer et al., 2018) suggest that the photic zone is characterized by a single fluorescence peak with a maximum at 110 m and which disappeared at 200 m (Figure S1C). Thus, we define the mesopelagic as beginning at 200 m at the oxic site. Turbidity followed chlorophyll concentration and did not have a peak in the mesopelagic (Figure S1D), unlike the ODZ site. There was a salinity peak at 150 m (Figure S1B).

553   Particle numbers were higher between the base of the photic zone through 1000 m at the ETNP ODZ site,

554   than at the same-latitude, oxygenic, P16 Station 100 (Figure S7A). Particle size distributions were similar

555   between the two sites above 500 m, being characterized by overlapping confidence intervals generated by

556   a general additive model. From 500 m to 1000 m, particle size distributions were flatter at the ETNP site,

557   being characterized by a smaller proportion of smaller particles, relative to larger ones (Figure S7B).

558   Microaggregate particles (100 μm - 500 μm) at the ETNP ODZ site were about two orders of magnitude

559   more common than marine snow particles (≥ 500 μm) (Figure S8). ≥500 μm particle numbers appeared

560   to attenuate more quickly than <500 μm particles, and more generally follow a power law decrease, while

561   <500 μm particles appeared to increase around 500 m depth. Flux was predicted to be predominantly

562   from <500 um, rather than ≥500 μm particles, at all depths except the shallowest depth bin in the surface

563   of the photic zone. The particle size distribution, calculated only on ≥500 μm particles, was more variable

564   between depths than calculated for <500 μm particles. Data from the oxic P16 Station 100 suggested

565   more particles, steeper particle size distribution, and more flux at this station than at the ETNP station.

566   They also suggested that differences between <500 μm and ≥ 500 μm particles, with respect to number,

567   flux and size distribution that were broadly similar to the ones seen at ETNP Station P2. In contrast to the

568   anoxic station, at the oxic station flux always decreased with depth (Figure S9A+B).

7   *Discussion*

7.1   **Diel migrators spend time in the ODZ core**

571   Organisms of all sizes appear to migrate into the core of the ODZ at our site. Most migrators appear to

572   leave the surface at dawn, spend the day in the top 500 m of the ODZ and return to the surface at dusk

573   (Figure 2A), while others show the opposite pattern, leaving the surface at dusk and returning at dawn

574   (Figure 2B). Diel migration is prevalent throughout the oceans (Cisewski et al., 2010; Hays, 2003;

575   Heywood, 1996; Jiang et al., 2007; Rabindranath et al., 2011; Sainmont et al., 2014; Yang et al., 2019),

576   including at other ODZ sites (Antezana, 2009; Kiko et al., 2020; Riquelme-Bugueño et al., 2020),

577   including highly anoxic sites with secondary, anoxic, deep chlorophyll maxima, like this one (Bianchi et

578   al., 2014; Hidalgo et al., 2005), and much of the ETNP ODZ (Herrera et al., 2019). Sampling efforts in

579   the Costa Rica Dome, a unique system in the ETNP, find that euphausiids and fish migrate into the ODZ

580   (Maas et al., 2014; Wishner et al., 2013), but that diel migrators are primarily 2 mm–5 mm in size

581   (Wishner et al., 2013). Krill in the Humboldt current OMZ similarly spend the day at depth and migrate to

582   the surface at night (Riquelme-Bugueño et al., 2020). The presence of organisms that appear and

583   disappear just above the base of the photic zone, in the region of the deeper anoxic fluorescence peak

584   region, but absence of a tell-tale signature of mass migration before or after they appear (Figure 2C) may

23

585   suggest that these organisms migrate at different times of the day to this deep region, rather than all at

586   once. Another possibility is that they pass through our station at this depth in mid-day, but migrate to

587   depth at another location.

588   The organisms that appear between 500 m and 1000 m (Figure 2E) have acoustic signatures that resemble

589   those of jellyfish (Kaartvedt et al., 2007), but could also represent other organisms such as salps (Maas et

590   al., 2014; Ressler, 2002). That they appear in horizontal bands that do not appear to trend upwards over

591   time suggests that these swarms are traveling through our site at progressively shallower depths over the

592   course of the day, but that the individual swarms are not themselves moving upward at this station. This

593   pattern suggests that any vertical migration by these organisms happens elsewhere or occurs more slowly

594   than the advection seen at this site. That they appear at different depths at different times of the day

595   suggest that these organisms have some sort of vertical migration pattern. Future work may consider more

596   highly resolved spatial and temporal monitoring of this phenomenon. Indeed molecular surveys have

597   found evidence of both Cnidarians and Ctenophores both within and below the ETSP ODZ near Chile

598   (Parris et al., 2014).

7.2 Flux is lower at this site than previous measurements in the ETNP

600   Flux at P2 was lower at all depths, ranging from 10–100 μmol/m^2/day, than was seen in previous

601   measurements by traps at other, more productive, ODZ sites, which ranged from 1000–

602   10000 μmol/m^2/day (Hartnett & Devol, 2003; Van Mooy et al., 2002).

7.3 The flux to size relationship is typical of other sites

604   The exponent of the particle size to flux relationship that we saw at our site (2.00) is of a similar

605   magnitude to, but slightly smaller than, those seen by other studies that compare UVP flux to trap flux

606   (Guidi et al., 2008; Kiko et al., 2020). Differences in the size-flux relationship could indicate that this

607   relationship truly varies between sites, or that imprecision in flux measurements leads to differences in

608   these values between studies. The single fit and relationship that we carried out does not account for

609   variation in the size to flux ratio across time and depth, nor does it account for differences in particles of

610   different origin. In practice, this value could change over depth and time. Setting up, deploying and

611   retrieving each trap array is a large effort. However, coupled particle flux and size measurements that are

612   more resolved with respect to depth, space or time might allow for further exploration of the

613   spatiotemporal variability of this relationship. In other systems, combined image analysis and gel traps

614   (McDonnell & Buesseler, 2010, 2012) have provided opportunities to explore particle size to flux

615   relationships and how they vary between particle types in more detail.

24

7.4   Remineralization rates of all particles decrease in the ODZ, but disaggregation does not

Particle size profiles, particle size distribution slopes, and estimated biovolume, averaged across all casts and smoothed, are all similar to the predictions made by Weber and Bianchi's (2020) "Model 1". (Figure 5), and therefore our hypothesis **H1**, that all particles are remineralized more slowly than in oxic sites. This suggests that the low oxygen at this site decreases the remineralization rate of all particles, including <500 μm microaggregates. It does not support the **H2** in which disaggregation is suppressed in the ODZ, nor **H3** in which only the very large particles' remineralization is slowed due to sulfate reduction. The data at the oxic site generally conformed to Weber and Bianchi's null model, "Model 0", which was their prediction for particle distributions at oxic sites (2020). However, one difference was that the observed particle size distribution, while essentially constant from the base of the photic zone through 1000 m, appeared to steepen between 1000 m and 2000 m, suggesting an increase in the abundance of <500 μm particles, relative to Model 0. This could indicate increased disaggregation in this region or horizontal transport of small particles through advection in this region. One possible source of disaggregation are zooplankton communities that have been found to specialize in feeding in the lower oxycline (Saltzman & Wishner, 1997; Wishner et al., 1995). These communities actively seek out the lower oxycline and feed on particles that have escaped remineralization in the ODZ, potentially resulting in the increased disaggregation we observe in this depth interval. Such a community would likely be comprised primarily of small organisms which the EK60 is not able to measure at this depth. One possible source of horizontal transport is colloids in a deep iron plume (Homoky et al., 2021; Lam et al., 2020).

7.5   Zooplankton likely transport organic matter into the ODZ core

Predicted flux levels sometimes increase between 275 m and 625 m, and at all other times attenuate very slowly in this region. The EK60 data suggest the diel migration of all sizes of organisms to this region, agreeing with previous analysis of copepods collected with nets (Wishner et al., 2020). Taken together, the concurrent intermittent increases in flux with diel migration in the top 500 m suggests that zooplankton are transporting organic matter. The observation that the rate of change in flux changes with depth suggests some day-to-day variability in this transport. That this rate does not vary statistically significantly between day and night suggests that any diel release of particles is relatively small compared to the particles already present in situ. Indeed, it suggests that particle sinking is slow enough that any particles that are transported to depth during the day are retained at night. Furthermore, nocturnal migrators are likely playing a role in carbon transport which may smooth out any diel signal. Another possibility, given that the magnitude of the day-to-day variability in apparent particle flux is small, is that

649 the zooplankton themselves, which likely make up about 5% of what the UVP counts as particles, may be
650 driving this apparent pattern and that particle flux itself does not vary. More likely, especially given the
651 observation that this flux variability did not track well with the within day backscattering patterns seen by
652 the EK60 and the small number of particles that are zooplankton, is that this factor accounts for some, but
653 not all, of the observed variability in flux. An additional source of temporal variability in flux is variation
654 in particle export from the photic zone. Zooplankton, if they are more common in large particle size bins,
655 or even if they have a flatter size distribution spectrum than non-living particles, may flatten the particle
656 size spectrum, where they are present. However, this effect, if present at our site, appears to be
657 overpowered by the disaggregation effect, since the particle size spectra appear to be steeper where
658 zooplankton are present.

659 Zooplankton are also known to congregate at the lower boundaries of ODZs (Wishner et al., 2018, 2020)
660 and high urea concentrations in the lower oxycline of the ETNP have been suggested to be due to these
661 zooplankton (Widner et al., 2018). Beam attenuation indicates a third peak in the oxycline below the
662 ODZ. We do not see this congregation in the EK60 data. However, it is possible that small organisms do
663 congregate here, but are not detected by the EK60's 12000 and 20000 kHZ signals, which do not
664 penetrate to 1000 m in our data. The EK60 data do however suggest that larger, krill to fish sized
665 organisms are not abundant in the lower oxycline.

7.6 Zooplankton likely disaggregate particles in the ODZ core

667 The observation that there is greater flux by microaggregate particles (< 500 μm) than would be predicted
668 by remineralization and sinking alone (Figure 7), between the photic zone and 500 m suggests that some
669 process is disaggregating large particles into smaller ones. That this apparent disaggregation corresponds
670 with the region where migratory organisms are found suggests that some of these organisms, likely small
671 animals such as copepods and euphausiids (Herrera et al., 2019; Maas et al., 2014), may break down
672 particles (Dilling & Alldredge, 2000; Goldthwait et al., 2005). While, in principle, other processes such as
673 horizontal advection of water containing <500 μm particles (Inthorn, 2005) could be responsible for this
674 increase in <500 μm particles, there is no reason to expect horizontal differences at this site, which is at
675 the core of the ODZ and far from shore.

676 Other deviations from model assumptions could alternatively explain the increase in <500 μm particles
677 relative to model predictions. In particular, smaller particles might break down more slowly than larger
678 ones, or sink more quickly for their size than expected, as has been seen elsewhere (McDonnell &
679 Buesseler, 2010). Our model assumes a spherical particle drag profile, such that the particle sinking speed
680 fractal dimension (γ) is one less than the particle size fractal dimension (α) (Cram et al., 2018; Guidi et

681   al., 2008), and that these two values sum to the particle flux fractal dimension. If any of these assumptions

682   do not hold, the magnitude of the values may differ.

683   In contrast to the upper ODZ core, there is an apparent flattening of the particle size distribution below

684   500 m, beyond the expected effects generated by particle remineralization. This could suggest

685   aggregation processes (Burd & Jackson, 2009). Indeed, aggregation could be occurring throughout the

686   ODZ core, but only exceed disaggregation in the lower ODZ region. Alternatively, in this region,

687   processes resembling Weber and Bianchi's (2020) Model 3, corresponding to **H3**, in which large particles

688   remineralize more slowly than larger ones could also occur. Like aggregation, such processes could be

689   occurring through the ODZ but are overwhelmed by the effects of disaggregation above 500 m.

7.7   Water mass changes may affect particle flux and size changes

691   The observation that particle flux begins to attenuate below 500 m more quickly than it does between the

692   base of the photic zone and 500 m could be explained in part by a shift in water mass at this depth where

693   AAIW begins to mix with NEPIW (Figure S2). The AAIW is suggested to have micromolar oxygen

694   concentrations, as compared to the NEPIW, such that a small contribution of AAIW can raise the oxygen

695   concentration (Evans et al., 2020). However, measurements taken at this station in 2012 observed zero

696   oxygen though 800 m with the highly sensitive STOX electrode, suggesting that oxygen, if present, is

697   below 4 nM (Tiano et al., 2014). It is conceivable that the AAIW has larger particle sizes and lower

698   particle abundance characteristics due to its having advected from different geographic regions than the

699   overlying water, but it is difficult to see why this would be the case as these water masses stay in the ODZ

700   region for years (DeVries et al., 2012) and particles have a much shorter residence time. In any case, the

701   NEPIW to AAIW transition coincides with the lower limit of the depth to which vertically migrating

702   zooplankton travel (Figure 2), and so we are not able to deconvolve the effects of water mass changes

703   from that of changes in zooplankton effects on particle characteristics.

704   The change in water mass between 13CW and NEPIW, around 250 m, in contrast, does not appear to

705   correspond to any apparent changes in particle flux or size. Thus, we would argue that any historical

706   effects of these water mass differences are likely to be small, and that active transport differences above

707   and below 500 m likely have a larger effect.

7.8   Oxic site differences

709   The oxic site provides validation that the patterns that we see at the ETNP are unique to the ODZ region,

710   and do not apply to a same latitude ODZ site. The particle size distribution slope varied little and there

711   was not an increase in particle mass in the oxic site, consistent with Weber and Bianchi's (2020) null

712   model (Figure S10), in which oxygen is not limiting and particle sizes are not affected by anoxia. In this

713 case, small particles break down more quickly in the oxic site than our site and so there is no small
714 particle excess in this region. Similarly, the higher flux attenuation in the oxic site (Figure S9A) suggests
715 that the differences in attenuation of all particle sizes by microbes at both sites do indeed drive differences
716 in flux profiles, and by extension transfer efficiency, between oxic and anoxic regions. The lack of
717 increases in flux at the oxic site (Figure S9B) suggest that active transport may play a greater role in the
718 anoxic region than elsewhere. The lack in apparent excess of small particles over model prediction
719 (Figure S9C) could either indicate less activity by zooplankton in this region, or perhaps that
720 remineralization of small particles quickly removes any small particles produced by zooplankton in this
721 region.

7.9   Future directions

723 We advocate exploring the relationships between particle size distribution, flux and acoustic signatures in
724 other parts of the ETNP and other ODZ regions. Expanded spatial analysis of particle size spectra in
725 ODZs would allow the community to confirm whether Weber and Bianchi's (2020) model **(H1)**, that
726 particles of all sizes break down more slowly in ODZs, applies elsewhere. Similarly, a clear next step is to
727 apply our disaggregation model to other ocean regions, perhaps using particle size data already collected
728 by other groups (Guidi et al., 2008; Kiko et al., 2017, 2020).

729 While the UVP characterizes dynamics of particles >100 μm, particles smaller than this range contribute
730 dramatically to carbon flux (Durkin et al., 2015), and so their size distribution matters as well. However,
731 at some point particles become small enough that they likely do not sink, and so exploring
732 remineralization and disaggregation of <500 μm microaggregate particles into non-sinking size classes
733 would provide valuable context to these measurements. In-situ pumped POC data from the GEOTRACES
734 program have been used to describe the dynamics of smaller particle size classes (Lam et al., 2011; Lam
735 & Marchal, 2015). Other sensors, such as coulter counters (Sheldon et al., 1972) and Laser In-Situ
736 Scattering transmissometers (Ahn & Grant, 2007) provide size resolved distribution information about
737 these smaller size classes of particles. Comparison between UVP data and past and ongoing (Siegel et al.,
738 2016) studies of the characteristics of <100 μm particles provide opportunities to better understand the
739 dynamics of the full range of particle sizes.

740 The image data collected by the UVP offers opportunities to quantify the abundance and taxonomic
741 distribution of the zooplankton that migrate into the mesopelagic, as well as the particle types within this
742 region. Identifying this visual data would have the added benefit of allowing researchers analyze particle
743 size spectra, rather than the sum of particles and zooplankton as we do here.

8 Conclusions

If ODZs expand in response to the changing climate, larger areas of the ocean are likely to resemble this environment, which is oligotrophic and has an oxygen deficient zone spanning most of the mesopelagic zone. Previous models and observations have suggested that ODZs are sites of efficient carbon transfer to the deep ocean (Cram et al., 2018; Hartnett & Devol, 2003; Van Mooy et al., 2002; Weber & Bianchi, 2020), and our data appear to support this contention. Indeed, the mechanism of efficient transfer appears to be slowing of particle remineralization, presumably from decreased microbial metabolism, with zooplankton playing an important role in both active particle transport and particle disaggregation.

Our data could potentially be used in conjunction with mechanistic models (e.g. Weber & Bianchi, 2020) to constrain the relative carbon oxidation rate by nitrate reduction, denitrification and sulfate reduction processes, which is currently poorly understood (Bristow, 2018). Furthermore, it appears that diel migratory organisms both disaggregate particles and transport carbon throughout the top 500 m of the water column. Day-to-day and within day variability in organic matter transport was evident, though overall patterns in particle size, flux and disaggregation appeared to be consistent over the course of the time-series. The change in particle abundance and size between 500 m and the bottom of the ODZ has implications for the free-living microbes living in this region. These microbes are likely particularly organic matter starved, and so these decaying particles are likely an important energy source for them. Our data highlights the heterogeneous nature of the ETNP ODZ with depth and indicates that more detailed sampling should be performed for rate and microbial measurements to properly extrapolate to the entire ODZ.

9 Acknowledgements

29

10 References

776 Ahn, J. H., & Grant, S. B. (2007). Size Distribution, Sources, and Seasonality of Suspended Particles in

777   Southern California Marine Bathing Waters. *Environmental Science & Technology*, *41*(3), 695–

778   702. https://doi.org/10.1021/es061960+

779 Andersen, L. N. (2001). The new Simrad EK60 scientific echo sounder system. *The Journal of the*

780   *Acoustical Society of America*, *109*(5), 2336–2336. https://doi.org/10.1121/1.4744207

781 Antezana, T. (2009). Species-specific patterns of diel migration into the Oxygen Minimum Zone by

782   euphausiids in the Humboldt Current Ecosystem. *Progress in Oceanography*, *83*(1), 228–236.

783   https://doi.org/10.1016/j.pocean.2009.07.039

784 Archibald, K. M., Siegel, D. A., & Doney, S. C. (2019). Modeling the Impact of Zooplankton Diel

785   Vertical Migration on the Carbon Export Flux of the Biological Pump. *Global Biogeochemical*

786   *Cycles*, *33*(2), 181–199. https://doi.org/10.1029/2018GB005983

787 Bianchi, D., Stock, C., Galbraith, E. D., & Sarmiento, J. L. (2013). Diel vertical migration: Ecological

788   controls and impacts on the biological pump in a one-dimensional ocean model. *Global*

789   *Biogeochemical Cycles*, *27*(2), 478–491. https://doi.org/10.1002/gbc.20031

790 Bianchi, D., Babbin, A. R., & Galbraith, E. D. (2014). Enhancement of anammox by the excretion of diel

791   vertical migrators. *Proceedings of the National Academy of Sciences*, *111*(44), 15653–15658.

792   https://doi.org/10.1073/pnas.1410790111

793 Bianchi, D., Weber, T. S., Kiko, R., & Deutsch, C. (2018). Global niche of marine anaerobic metabolisms

794   expanded by particle microenvironments. *Nature Geoscience*, *11*(4), 263.

795   https://doi.org/10.1038/s41561-018-0081-0

796 Boyer, T., Garcia, H. E., Locarini, R. A., Ricardo, A., Zweng, M. M., Mishonov, A. V., et al. (2018).

797   *World Ocean Atlas 2018*. NOAA National Centers for Environmntal Information.

798   Briggs, N., Dall'Olmo, G., & Claustre, H. (2020). Major role of particle fragmentation in regulating

799   biological sequestration of CO2 by the oceans. *Science*, *367*(6479), 791–793.

800   https://doi.org/10.1126/science.aay1790

801   Bristow, L. A. (2018). Anoxia in the snow. *Nature Geoscience*, *11*(4), 226–227.

802   https://doi.org/10.1038/s41561-018-0088-6

803   Buonassissi, C. J., & Dierssen, H. M. (2010). A regional comparison of particle size distributions and the

804   power law approximation in oceanic and estuarine surface waters. *Journal of Geophysical*

805   *Research: Oceans*, *115*(C10). https://doi.org/10.1029/2010JC006256

806   Burd, A. B., & Jackson, G. A. (2009). Particle Aggregation. *Annual Review of Marine Science*, *1*(1), 65–

807   90. https://doi.org/10.1146/annurev.marine.010908.163904

808   Cavan, E. L., Trimmer, M., Shelley, F., & Sanders, R. (2017). Remineralization of particulate organic

809   carbon in an ocean oxygen minimum zone. *Nature Communications*, *8*, 14847.

810   https://doi.org/10.1038/ncomms14847

811   Cisewski, B., Strass, V. H., Rhein, M., & Krägefsky, S. (2010). Seasonal variation of diel vertical

812   migration of zooplankton from ADCP backscatter time series data in the Lazarev Sea, Antarctica.

813   *Deep Sea Research Part I: Oceanographic Research Papers*, *57*(1), 78–94.

814   https://doi.org/10.1016/j.dsr.2009.10.005

815   Cram, J. A., Weber, T., Leung, S. W., McDonnell, A. M. P., Liang, J.-H., & Deutsch, C. (2018). The Role

816   of Particle Size, Ballast, Temperature, and Oxygen in the Sinking Flux to the Deep Sea. *Global*

817   *Biogeochemical Cycles*, *32*(5), 858–876. https://doi.org/10.1029/2017GB005710

818   Date, S. (2020, November 21). Generalized Linear Models. Retrieved May 2, 2021, from

819   https://towardsdatascience.com/generalized-linear-models-9ec4dfe3dc3f

820   Deutsch, C., Berelson, W., Thunell, R., Weber, T., Tems, C., McManus, J., et al. (2014). Centennial

821   changes in North Pacific anoxia linked to tropical trade winds. *Science*, *345*(6197), 665–668.

822   https://doi.org/10.1126/science.1252332

31

823   DeVries, T., & Weber, T. (2017). The export and fate of organic matter in the ocean: New constraints

824   from combining satellite and oceanographic tracer observations. *Global Biogeochemical Cycles*,

825   2016GB005551. https://doi.org/10.1002/2016GB005551

826   DeVries, T., Deutsch, C., Primeau, F., Chang, B., & Devol, A. (2012). Global rates of water-column

827   denitrification derived from nitrogen gas measurements. *Nature Geoscience*, *5*(8), 547–550.

828   https://doi.org/10.1038/ngeo1515

829   DeVries, T., Liang, J.-H., & Deutsch, C. (2014). A mechanistic particle flux model applied to the oceanic

830   phosphorus cycle. *Biogeosciences Discuss.*, *11*(3), 3653–3699. https://doi.org/10.5194/bgd-11-

831   3653-2014

832   Dilling, L., & Alldredge, A. L. (2000). Fragmentation of marine snow by swimming macrozooplankton:

833   A new process impacting carbon cycling in the sea. *Deep Sea Research Part I: Oceanographic

834   Research Papers*, *47*(7), 1227–1245. https://doi.org/10.1016/S0967-0637(99)00105-3

835   Durkin, C. A., Estapa, M. L., & Buesseler, K. O. (2015). Observations of carbon export by small sinking

836   particles in the upper mesopelagic. *Marine Chemistry*, *175*, 72–81.

837   https://doi.org/10.1016/j.marchem.2015.02.011

838   Evans, N., Boles, E., Kwiecinski, J. V., Mullen, S., Wolf, M., Devol, A. H., et al. (2020). The role of

839   water masses in shaping the distribution of redox active compounds in the Eastern Tropical North

840   Pacific oxygen deficient zone and influencing low oxygen concentrations in the eastern Pacific

841   Ocean. *Limnology and Oceanography*, *65*(8), 1688–1705. https://doi.org/10.1002/lno.11412

842   Francois, R., Honjo, S., Krishfield, R., & Manganini, S. (2002). Factors controlling the flux of organic

843   carbon to the bathypelagic zone of the ocean. *Global Biogeochemical Cycles*, *16*(4), 34-1-34–20.

844   https://doi.org/10.1029/2001GB001722

845   Fuchsman, C. A., Devol, A. H., Saunders, J. K., McKay, C., & Rocap, G. (2017). Niche Partitioning of

846   the N Cycling Microbial Community of an Offshore Oxygen Deficient Zone. *Frontiers in

847   Microbiology*, *8*. https://doi.org/10.3389/fmicb.2017.02384

848   Fuchsman, C. A., Palevsky, H. I., Widner, B., Duffy, M., Carlson, M. C. G., Neibauer, J. A., et al. (2019).

849   Cyanobacteria and cyanophage contributions to carbon and nitrogen cycling in an oligotrophic

850   oxygen-deficient zone. *The ISME Journal*, 1. https://doi.org/10.1038/s41396-019-0452-6

851   Garcia-Robledo, E., Padilla, C. C., Aldunate, M., Stewart, F. J., Ulloa, O., Paulmier, A., et al. (2017).

852   Cryptic oxygen cycling in anoxic marine zones. *Proceedings of the National Academy of*

853   *Sciences*, *114*(31), 8319–8324. https://doi.org/10.1073/pnas.1619844114

854   Goldthwait, S. A., Carlson, C. A., Henderson, G. K., & Alldredge, A. L. (2005). Effects of physical

855   fragmentation on remineralization of marine snow. *Marine Ecology Progress Series*, *305*, 59–65.

856   Guidi, L., Jackson, G. A., Stemmann, L., Miquel, J. C., Picheral, M., & Gorsky, G. (2008). Relationship

857   between particle size distribution and flux in the mesopelagic zone. *Deep Sea Research Part I:*

858   *Oceanographic Research Papers*, *55*(10), 1364–1374. https://doi.org/10.1016/j.dsr.2008.05.014

859   Hannides, C. C. S., Landry, M. R., Benitez-Nelson, C. R., Styles, R. M., Montoya, J. P., & Karl, D. M.

860   (2009). Export stoichiometry and migrant-mediated flux of phosphorus in the North Pacific

861   Subtropical Gyre. *Deep Sea Research Part I: Oceanographic Research Papers*, *56*(1), 73–88.

862   https://doi.org/10.1016/j.dsr.2008.08.003

863   Hartnett, H. E., & Devol, A. H. (2003). Role of a strong oxygen-deficient zone in the preservation and

864   degradation of organic matter: a carbon budget for the continental margins of northwest Mexico

865   and Washington State. *Geochimica et Cosmochimica Acta*, *67*(2), 247–264.

866   https://doi.org/10.1016/S0016-7037(02)01076-1

867   Hays, G. C. (2003). A review of the adaptive significance and ecosystem consequences of zooplankton

868   diel vertical migrations. In M. B. Jones, A. Ingólfsson, E. Ólafsson, G. V. Helgason, K.

869   Gunnarsson, & J. Svavarsson (Eds.), *Migrations and Dispersal of Marine Organisms* (pp. 163–

870   170). Dordrecht: Springer Netherlands. https://doi.org/10.1007/978-94-017-2276-6_18

871   Herrera, I., Yebra, L., Antezana, T., Giraldo, A., Färber-Lorda, J., & Hernández-León, S. (2019). Vertical

872   variability of Euphausia distinguenda metabolic rates during diel migration into the oxygen

873   minimum zone of the Eastern Tropical Pacific off Mexico. *Journal of Plankton Research*, *41*(2),

874   165–176. https://doi.org/10.1093/plankt/fbz004

875 Heywood, K. J. (1996). Diel vertical migration of zooplankton in the Northeast Atlantic. *Journal of*

876   *Plankton Research*, *18*(2), 163–184. https://doi.org/10.1093/plankt/18.2.163

877 Hidalgo, P., Escribano, R., & Morales, C. E. (2005). Ontogenetic vertical distribution and diel migration

878   of the copepod Eucalanus inermis in the oxygen minimum zone off northern Chile (20–21° S).

879   *Journal of Plankton Research*, *27*(6), 519–529. https://doi.org/10.1093/plankt/fbi025

880 Homoky, W. B., Conway, T. M., John, S. G., König, D., Deng, F., Tagliabue, A., & Mills, R. A. (2021).

881   Iron colloids dominate sedimentary supply to the ocean interior. *Proceedings of the National*

882   *Academy of Sciences*, *118*(13), e2016078118. https://doi.org/10.1073/pnas.2016078118

883 Horak, R. E. A., Ruef, W., Ward, B. B., & Devol, A. H. (2016). Expansion of denitrification and anoxia

884   in the eastern tropical North Pacific from 1972 to 2012. *Geophysical Research Letters*, *43*(10),

885   2016GL068871. https://doi.org/10.1002/2016GL068871

886 Inthorn, M. (2005). Lateral particle transport in nepheloid layers - a key factor for organic matter

887   distribution and quality in the Benguela high-productivity area. Retrieved from

888   https://media.suub.uni-bremen.de/handle/elib/2212

889 Ito, T., Minobe, S., Long, M. C., & Deutsch, C. (2017). Upper ocean O_2 trends: 1958-2015. *Geophysical*

890   *Research Letters*, *44*(9), 4214–4223. https://doi.org/10.1002/2017GL073613

891 Jackson, G. A., & Burd, A. B. (2001). A model for the distribution of particle flux in the mid-water

892   column controlled by subsurface biotic interactions. *Deep Sea Research Part II: Topical Studies*

893   *in Oceanography*, *49*(1), 193–217. https://doi.org/10.1016/S0967-0645(01)00100-X

894 Jiang, S., Dickey, T. D., Steinberg, D. K., & Madin, L. P. (2007). Temporal variability of zooplankton

895   biomass from ADCP backscatter time series data at the Bermuda Testbed Mooring site. *Deep Sea*

896   *Research Part I: Oceanographic Research Papers*, *54*(4), 608–636.

897   https://doi.org/10.1016/j.dsr.2006.12.011

898   Kaartvedt, S., Klevjer, T. A., Torgersen, T., Sørnes, T. A., & Røstad, A. (2007). Diel vertical migration of

899   individual jellyfish (Periphylla periphylla). *Limnology and Oceanography*, *52*(3), 975–983.

900   https://doi.org/10.4319/lo.2007.52.3.0975

901   Keil, R. G., Neibauer, J. A., & Devol, A. H. (2016). A multiproxy approach to understanding the

902   "enhanced" flux of organic matter through the oxygen-deficient waters of the Arabian Sea.

903   *Biogeosciences*, *13*(7), 2077–2092. http://dx.doi.org/10.5194/bg-13-2077-2016

904   Kiko, R., Biastoch, A., Brandt, P., Cravatte, S., Hauss, H., Hummels, R., et al. (2017). Biological and

905   physical influences on marine snowfall at the equator. *Nature Geoscience*, *10*(11), 852–858.

906   https://doi.org/10.1038/ngeo3042

907   Kiko, R., Brandt, P., Christiansen, S., Faustmann, J., Kriest, I., Rodrigues, E., et al. (2020). Zooplankton-

908   Mediated Fluxes in the Eastern Tropical North Atlantic. *Frontiers in Marine Science*, *7*.

909   https://doi.org/10.3389/fmars.2020.00358

910   Kwon, E. Y., & Primeau, F. (2008). Optimization and sensitivity of a global biogeochemistry ocean

911   model using combined in situ DIC, alkalinity, and phosphate data. *Journal of Geophysical*

912   *Research: Oceans*, *113*(C8), C08011. https://doi.org/10.1029/2007JC004520

913   Lam, P., & Kuypers, M. M. M. (2011). Microbial Nitrogen Cycling Processes in Oxygen Minimum

914   Zones. *Annual Review of Marine Science*, *3*(1), 317–345. https://doi.org/10.1146/annurev-marine-

915   120709-142814

916   Lam, P. J., & Marchal, O. (2015). Insights into Particle Cycling from Thorium and Particle Data. *Annual*

917   *Review of Marine Science*, *7*(1), 159–184. https://doi.org/10.1146/annurev-marine-010814-

918   015623

919   Lam, P. J., Doney, S. C., & Bishop, J. K. B. (2011). The dynamic ocean biological pump: Insights from a

920   global compilation of particulate organic carbon, CaCO3 , and opal concentration profiles from

921   the mesopelagic. *Global Biogeochemical Cycles*, *25*(3), n/a-n/a.

922   https://doi.org/10.1029/2010GB003868

923   Lam, P. J., Heller, M. I., Lerner, P. E., Moffett, J. W., & Buck, K. N. (2020). Unexpected Source and

924   Transport of Iron from the Deep Peru Margin. *ACS Earth and Space Chemistry*, *4*(7), 977–992.

925   https://doi.org/10.1021/acsearthspacechem.0c00066

926   Lampitt, R. S., Noji, T., & von Bodungen, B. (1990). What happens to zooplankton faecal pellets?

927   Implications for material flux. *Marine Biology*, *104*(1), 15–23.

928   https://doi.org/10.1007/BF01313152

929   Lee, W.-J., Staneva, V., Mayorga, E., Nguyen, K., Satiewan, L., & Majeed, I. (2021). Echopype:

930   Enhancing the interoperability and scalability of ocean sonar data processing. *The Journal of the*

931   *Acoustical Society of America*, *149*(4), A63–A63. https://doi.org/10.1121/10.0004522

932   Maas, A. E., Frazar, S. L., Outram, D. M., Seibel, B. A., & Wishner, K. F. (2014). Fine-scale vertical

933   distribution of macroplankton and micronekton in the Eastern Tropical North Pacific in

934   association with an oxygen minimum zone. *Journal of Plankton Research*, *36*(6), 1557–1575.

935   https://doi.org/10.1093/plankt/fbu077

936   McDonnell, A. M. P., & Buesseler, K. O. (2010). Variability in the average sinking velocity of marine

937   particles. *Limnology and Oceanography*, *55*(5), 2085–2096.

938   https://doi.org/10.4319/lo.2010.55.5.2085

939   McDonnell, A. M. P., & Buesseler, K. O. (2012). A new method for the estimation of sinking particle

940   fluxes from measurements of the particle size distribution, average sinking velocity, and carbon

941   content. *Limnology and Oceanography: Methods*, *10*(5), 329–346.

942   https://doi.org/10.4319/lom.2012.10.329

943   Neuer, S., Iversen, M., & Fischer, G. (2014). The Ocean's Biological Carbon pump as part of the global

944   Carbon Cycle. *Limnology and Oceanography E-Lectures*, *4*(4), 1–51.

945   https://doi.org/10.4319/lol.2014.sneuer.miversen.gfischer.9

946   Noji, T. T., Estep, K. W., Macintyre, F., & Norrbin, F. (1991). Image Analysis of Faecal Material Grazed

947   Upon by Three Species Of Copepods: Evidence For Coprorhexy, Coprophagy and Coprochaly.

948   *Journal of the Marine Biological Association of the United Kingdom*, *71*(2), 465–480.

949   https://doi.org/10.1017/S0025315400051717

950   Ooi, H. (2013, August 8). Where does the offset go in Poisson/negative binomial regression? Retrieved

951   May 2, 2021, from https://stats.stackexchange.com/questions/66791/where-does-the-offset-go-in-

952   poisson-negative-binomial-regression

953   Parris, D. J., Ganesh, S., Edgcomb, V. P., DeLong, E. F., & Stewart, F. J. (2014). Microbial eukaryote

954   diversity in the marine oxygen minimum zone off northern Chile. *Frontiers in Microbiology*, *5*.

955   https://doi.org/10.3389/fmicb.2014.00543

956   Passow, U., & Carlson, C. (2012). The biological pump in a high CO2 world. *Marine Ecology Progress*

957   *Series*, *470*, 249–271. https://doi.org/10.3354/meps09985

958   Pavia, F. J., Anderson, R. F., Lam, P. J., Cael, B. B., Vivancos, S. M., Fleisher, M. Q., et al. (2019).

959   Shallow particulate organic carbon regeneration in the South Pacific Ocean. *Proceedings of the*

960   *National Academy of Sciences*, *116*(20), 9753–9758. https://doi.org/10.1073/pnas.1901863116

961   Pennington, J. T., Mahoney, K. L., Kuwahara, V. S., Kolber, D. D., Calienes, R., & Chavez, F. P. (2006).

962   Primary production in the eastern tropical Pacific: A review. *Progress in Oceanography*, *69*(2–4),

963   285–317. https://doi.org/10.1016/j.pocean.2006.03.012

964   Peterson, M. L., Wakeham, S. G., Lee, C., Askea, M. A., & Miquel, J. C. (2005). Novel techniques for

965   collection of sinking particles in the ocean and determining their settling rates. *Limnology and*

966   *Oceanography: Methods*, *3*(12), 520–532. https://doi.org/10.4319/lom.2005.3.520

967   Picheral, M., Guidi, L., Stemmann, L., Karl, D. M., Iddaoud, G., & Gorsky, G. (2010). The Underwater

968   Vision Profiler 5: An advanced instrument for high spatial resolution studies of particle size

969   spectra and zooplankton. *Limnology and Oceanography: Methods*, *8*(9), 462–473.

970   https://doi.org/10.4319/lom.2010.8.462

971   Picheral, M., Colin, S., & Irisson, J.-O. (2017). *EcoTaxa, a tool for the taxonomic classification of*

972   *images*. Retrieved from http://ecotaxa.obs-vlfr.fr

973   Poulsen, L., & Kiørboe, T. (2005). Coprophagy and coprorhexy in the copepods Acartia tonsa and

974   Temora longicornis: clearance rates and feeding behaviour. *Marine Ecology Progress Series*, *299*,

975   217–227. https://doi.org/10.3354/meps299217

976   Rabindranath, A., Daase, M., Falk-Petersen, S., Wold, A., Wallace, M. I., Berge, J., & Brierley, A. S.

977   (2011). Seasonal and diel vertical migration of zooplankton in the High Arctic during the autumn

978   midnight sun of 2008. *Marine Biodiversity*, *41*(3), 365–382. https://doi.org/10.1007/s12526-010-

979   0067-7

980   Raven, M. R., Keil, R. G., & Webb, S. M. (2021). Microbial sulfate reduction and organic sulfur

981   formation in sinking marine particles. *Science*, *371*(6525), 178–181.

982   https://doi.org/10.1126/science.abc6035

983   Ressler, P. H. (2002). Acoustic backscatter measurements with a 153kHz ADCP in the northeastern Gulf

984   of Mexico: determination of dominant zooplankton and micronekton scatterers. *Deep Sea*

985   *Research Part I: Oceanographic Research Papers*, *49*(11), 2035–2051.

986   https://doi.org/10.1016/S0967-0637(02)00117-6

987   Riquelme-Bugueño, R., Pérez-Santos, I., Alegría, N., Vargas, C. A., Urbina, M. A., & Escribano, R.

988   (2020). Diel vertical migration into anoxic and high- pCO_2 waters: acoustic and net-based krill

989   observations in the Humboldt Current. *Scientific Reports*, *10*(1), 17181.

990   https://doi.org/10.1038/s41598-020-73702-z

991   Rocap, G., Keil, R., Devol, A., & Deutsch, C. (2017). *Water temperature, salinity, and other data from*

992   *CTD taken from the RV Sikuliaq in the Pacific Ocean between San Diego, California and*

993   *Manzanillo, Mexico from 2016-12-21 to 2017-01-13 (NCEI Accession 0164968). [Temperature,*

994   *Salinity, Oxygen, Beam Attenuation, Fluorescence, PAR].* NOAA National Centers for

995   Environmental Information. Retrieved from https://accession.nodc.noaa.gov/0164968

996   Roullier, F., Berline, L., Guidi, L., Durrieu De Madron, X., Picheral, M., Sciandra, A., et al. (2014).

997   Particle size distribution and estimated carbon flux across the Arabian Sea oxygen minimum

998   zone. *Biogeosciences*, *11*(16), 4541–4557. https://doi.org/10.5194/bg-11-4541-2014

38

999   Sainmont, J., Gislason, A., Heuschele, J., Webster, C. N., Sylvander, P., Wang, M., & Varpe, Ø. (2014).

1000   Inter- and intra-specific diurnal habitat selection of zooplankton during the spring bloom

1001   observed by Video Plankton Recorder. *Marine Biology*, *161*(8), 1931–1941.

1002   https://doi.org/10.1007/s00227-014-2475-x

1003   Saltzman, J., & Wishner, K. F. (1997). Zooplankton ecology in the eastern tropical Pacific oxygen

1004   minimum zone above a seamount: 2. Vertical distribution of copepods. *Deep Sea Research Part*

1005   *I: Oceanographic Research Papers*, *44*(6), 931–954. https://doi.org/10.1016/S0967-

1006   0637(97)00006-X

1007   Saunders, J. K., Fuchsman, C. A., McKay, C., & Rocap, G. (2019). Complete arsenic-based respiratory

1008   cycle in the marine microbial communities of pelagic oxygen-deficient zones. *Proceedings of the*

1009   *National Academy of Sciences*, *116*(20), 9925–9930. https://doi.org/10.1073/pnas.1818349116

1010   Schmidtko, S., Stramma, L., & Visbeck, M. (2017). Decline in global oceanic oxygen content during the

1011   past five decades. *Nature*, *542*(7641), 335–341. https://doi.org/10.1038/nature21399

1012   Seibel, B. A. (2011). Critical oxygen levels and metabolic suppression in oceanic oxygen minimum

1013   zones. *Journal of Experimental Biology*, *214*(2), 326–336. https://doi.org/10.1242/jeb.049171

1014   Sheldon, R. W., Prakash, A., & Sutcliffe Jr., W. H. (1972). The Size Distribution of Particles in the

1015   Ocean. *Limnology and Oceanography*, *17*(3), 327–340. https://doi.org/10.4319/lo.1972.17.3.0327

1016   Siegel, D. A., Buesseler, K. O., Behrenfeld, M. J., Benitez-Nelson, C. R., Boss, E., Brzezinski, M. A., et

1017   al. (2016). Prediction of the Export and Fate of Global Ocean Net Primary Production: The

1018   EXPORTS Science Plan. *Frontiers in Marine Science*, *3*.

1019   https://doi.org/10.3389/fmars.2016.00022

1020   Simon, M., Grossart, H., Schweitzer, B., & Ploug, H. (2002). Microbial ecology of organic aggregates in

1021   aquatic ecosystems. *Aquatic Microbial Ecology*, *28*(2), 175–211.

1022   https://doi.org/10.3354/ame028175

1023   Steinberg, D. K., & Landry, M. R. (2017). Zooplankton and the Ocean Carbon Cycle. *Annual Review of*

1024   *Marine Science*, *9*, 413–444. https://doi.org/10.1146/annurev-marine-010814-015924

1025 Steinberg, D. K., Carlson, C. A., Bates, N. R., Goldthwait, S. A., Madin, L. P., & Michaels, A. F. (2000).

1026 Zooplankton vertical migration and the active transport of dissolved organic and inorganic carbon

1027 in the Sargasso Sea. *Deep Sea Research Part I: Oceanographic Research Papers*, *47*(1), 137–

1028 158. https://doi.org/10.1016/S0967-0637(99)00052-7

1029 Stramma, L., Johnson, G. C., Sprintall, J., & Mohrholz, V. (2008). Expanding Oxygen-Minimum Zones

1030 in the Tropical Oceans. *Science*, *320*(5876), 655–658. https://doi.org/10.1126/science.1153847

1031 Stukel, M. R., Décima, M., Landry, M. R., & Selph, K. E. (2018). Nitrogen and Isotope Flows Through

1032 the Costa Rica Dome Upwelling Ecosystem: The Crucial Mesozooplankton Role in Export Flux.

1033 *Global Biogeochemical Cycles*, *32*(12), 1815–1832. https://doi.org/10.1029/2018GB005968

1034 Stukel, M. R., Ohman, M. D., Kelly, T. B., & Biard, T. (2019). The Roles of Suspension-Feeding and

1035 Flux-Feeding Zooplankton as Gatekeepers of Particle Flux Into the Mesopelagic Ocean in the

1036 Northeast Pacific. *Frontiers in Marine Science*, *6*. https://doi.org/10.3389/fmars.2019.00397

1037 Tiano, L., Garcia-Robledo, E., Dalsgaard, T., Devol, A. H., Ward, B. B., Ulloa, O., et al. (2014). Oxygen

1038 distribution and aerobic respiration in the north and south eastern tropical Pacific oxygen

1039 minimum zones. *Deep Sea Research Part I: Oceanographic Research Papers*, *94*, 173–183.

1040 https://doi.org/10.1016/j.dsr.2014.10.001

1041 Turner, J. T. (2015). Zooplankton fecal pellets, marine snow, phytodetritus and the ocean's biological

1042 pump. *Progress in Oceanography*, *130*, 205–248. https://doi.org/10.1016/j.pocean.2014.08.005

1043 Van Mooy, B. A. S., Keil, R. G., & Devol, A. H. (2002). Impact of suboxia on sinking particulate organic

1044 carbon: Enhanced carbon flux and preferential degradation of amino acids via denitrification.

1045 *Geochimica et Cosmochimica Acta*, *66*(3), 457–465. https://doi.org/10.1016/S0016-

1046 7037(01)00787-6

1047 Weber, T., & Bianchi, D. (2020). Efficient Particle Transfer to Depth in Oxygen Minimum Zones of the

1048 Pacific and Indian Oceans. *Frontiers in Earth Science*, *8*.

1049 https://doi.org/10.3389/feart.2020.00376

40

1050   Widner, B., Fuchsman, C. A., Chang, B. X., Rocap, G., & Mulholland, M. R. (2018). Utilization of urea

1051   and cyanate in waters overlying and within the eastern tropical north Pacific oxygen deficient

1052   zone. *FEMS Microbiology Ecology*, *94*(10). https://doi.org/10.1093/femsec/fiy138

1053   Wilson, S. E., Steinberg, D. K., & Buesseler, K. O. (2008). Changes in fecal pellet characteristics with

1054   depth as indicators of zooplankton repackaging of particles in the mesopelagic zone of the

1055   subtropical and subarctic North Pacific Ocean. *Deep Sea Research Part II: Topical Studies in*

1056   *Oceanography*, *55*(14–15), 1636–1647. https://doi.org/10.1016/j.dsr2.2008.04.019

1057   Wishner, K. F., Ashjian, C. J., Gelfman, C., Gowing, M. M., Kann, L., Levin, L. A., et al. (1995). Pelagic

1058   and benthic ecology of the lower interface of the Eastern Tropical Pacific oxygen minimum zone.

1059   *Deep Sea Research Part I: Oceanographic Research Papers*, *42*(1), 93–115.

1060   https://doi.org/10.1016/0967-0637(94)00021-J

1061   Wishner, K. F., Outram, D. M., Seibel, B. A., Daly, K. L., & Williams, R. L. (2013). Zooplankton in the

1062   eastern tropical north Pacific: Boundary effects of oxygen minimum zone expansion. *Deep Sea*

1063   *Research Part I: Oceanographic Research Papers*, *79*, 122–140.

1064   https://doi.org/10.1016/j.dsr.2013.05.012

1065   Wishner, K. F., Seibel, B. A., Roman, C., Deutsch, C., Outram, D., Shaw, C. T., et al. (2018). Ocean

1066   deoxygenation and zooplankton: Very small oxygen differences matter. *Science Advances*, *4*(12),

1067   eaau5180. https://doi.org/10.1126/sciadv.aau5180

1068   Wishner, K. F., Seibel, B., & Outram, D. (2020). Ocean deoxygenation and copepods: coping with

1069   oxygen minimum zone variability. *Biogeosciences*, *17*(8), 2315–2339. https://doi.org/10.5194/bg-

1070   17-2315-2020

1071   Yang, C., Xu, D., Chen, Z., Wang, J., Xu, M., Yuan, Y., & Zhou, M. (2019). Diel vertical migration of

1072   zooplankton and micronekton on the northern slope of the South China Sea observed by a moored

1073   ADCP. *Deep Sea Research Part II: Topical Studies in Oceanography*, *167*, 93–104.

1074   https://doi.org/10.1016/j.dsr2.2019.04.012

1075

1   Supporting Information for

2   **Slow particle remineralization, rather than suppressed**

3   **disaggregation, drives efficient flux transfer through the**

4   **Eastern Tropical North Pacific Oxygen Deficient Zone**

5

6   Jacob A. Cram[1], Clara A. Fuchsman[1], Megan E. Duffy[2], Jessica L. Pretty[3], Rachel M.

7   Lekanoff[3], Jacquelyn A Neibauer[2], Shirley W. Leung[2], Klaus B. Huebert[1], Thomas S.

8   Weber[4], Daniele Bianchi[5], Natalya Evans[6], Allan H. Devol[2], Richard G. Keil[2], Andrew

9   M.P. McDonnell[3]

10

11   [1]Horn Point Laboratory, University of Maryland Center for Environmental Science,

12   Cambridge, MD, USA.

13   [2]School of Oceanography, University of Washington Seattle, Seattle, WA, USA.

14   [3]College of Fisheries and Ocean Sciences, University of Alaska Fairbanks, Fairbanks,

15   AK, USA.

16   [4]School of Arts and Sciences, University of Rochester, Rochester, NY, USA.

17   [5]Department of Atmospheric and Oceanic Sciences, University of California Los

18   Angeles, Los Angeles, CA, USA.

19   [6]Department of Biological Sciences, University of Southern California, Los Angeles, CA,

20   USA.

21

22   Contents of this file

23

24   Figures S1 to S12

25   Caption for Text S1

26

27   Additional Supporting Information (Files uploaded separately)

28

29   Text S1

1

30 Introduction

31 This file contains supplemental figures referenced in the manuscript. It also contains a

32 caption for a .PDF file containing mathematical equations underpinning the particle

33 remineralization model used.

34
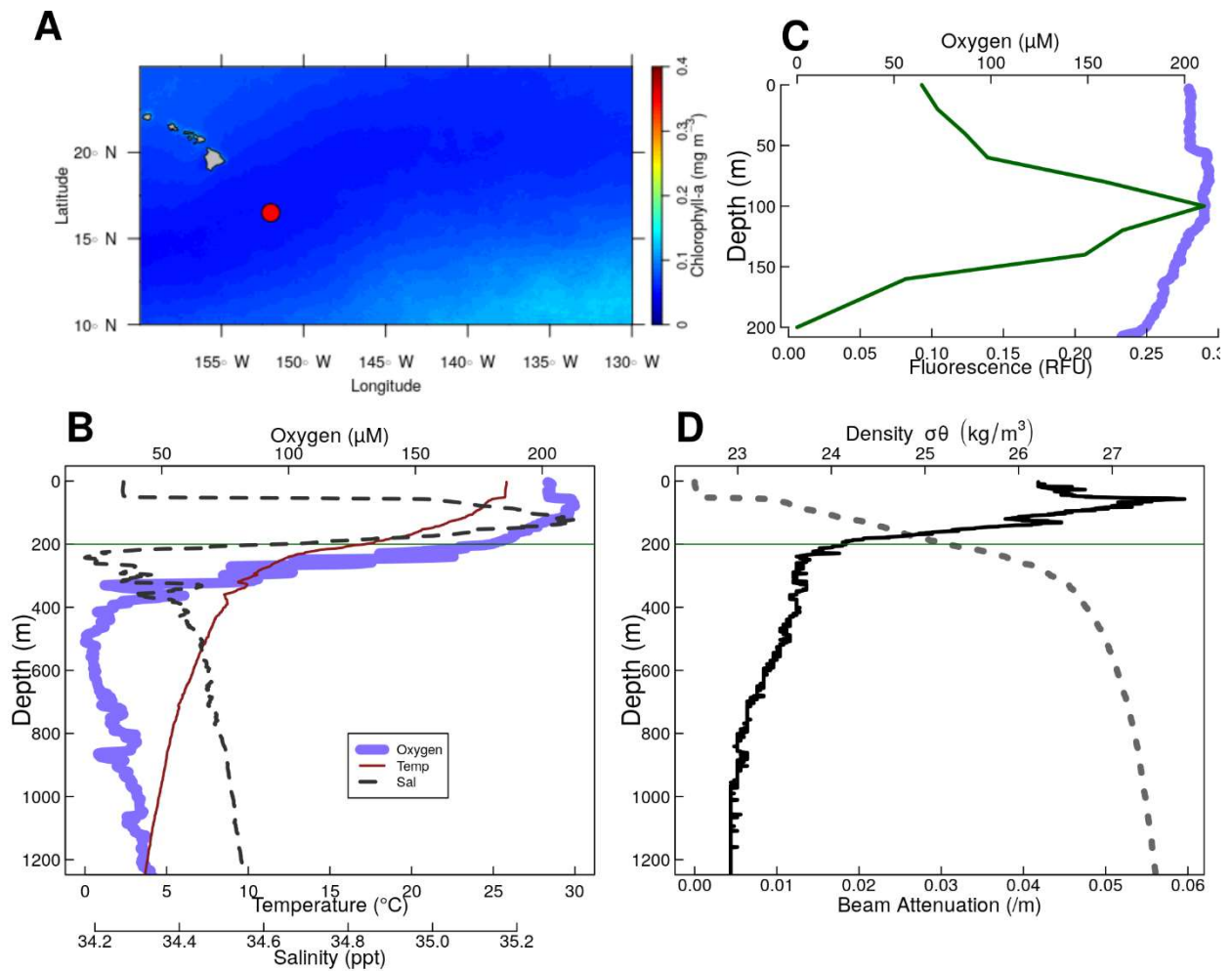
Figure S1. Physical and chemical data from P16 Station 100. Located at 16.5°N
152.0°W. (A) Map of the nearby tropical pacific station P16 Station 100. Colors indicate
chlorophyll concentrations at the surface, averaged over all MODIS images. The red
circle indicates the location of P16 Station 100. (B-D) Oceanographic parameters. The
thin horizontal green line shows the location of the base of the photic zone (200 m). (B)
Oxygen temperature and salinity. (C) Oxygen, and fluorescence. Because the fluorometer
was broken on this cruise, fluorescence data were pulled from world ocean atlas (Garcia
et al. 2014). (D) Beam attenuation and density, calculated from the salinity temperature
and pressure data.

3
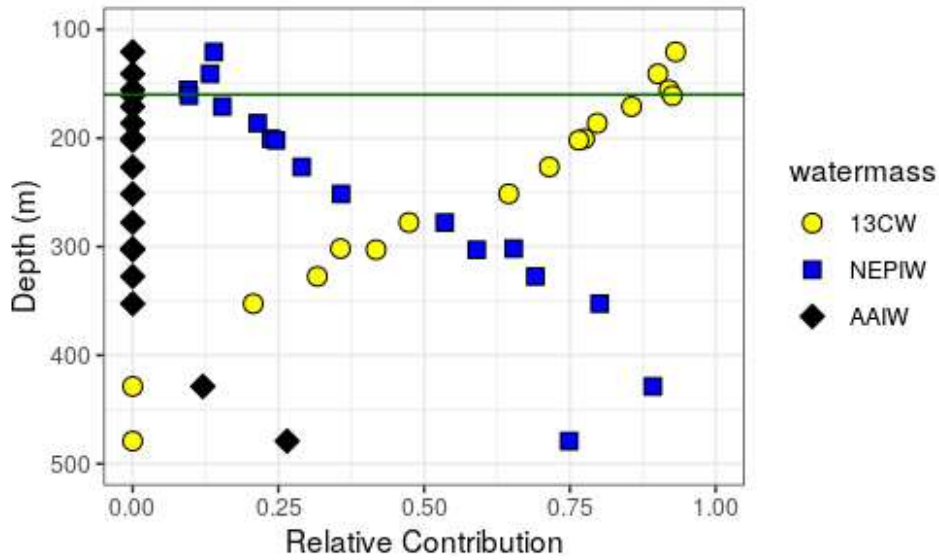
Figure S2. Water mass analysis at ETNP Station P2 indicates the relative contributions proportions of the three primary water masses at this site, $13°C$ water (13CW), North Equatorial Pacific Intermediate Water (NEPIW) and Antarctic Intermediate Water (AAIW). Values indicate relative contributions of each water mass and are scaled so as to sum to one. The horizontal green line indicates the base of the photic zone (160m). Data are taken directly from Evans et al. (2020).

4

52
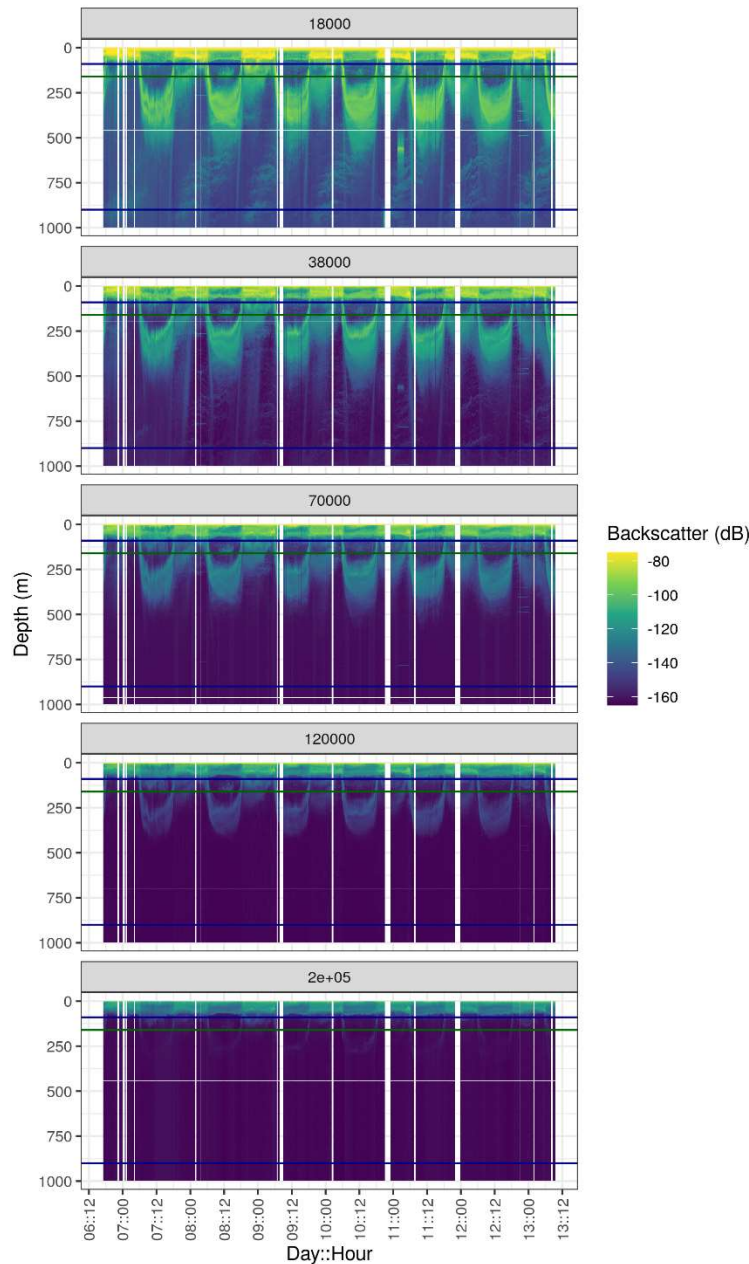
Figure S3. Acoustic data, measured by EK60, measured over the course of the

experiment, at ETNP Station P2. Shown are data from all frequency bands. Values are in

return signal intensity and have not been normalized to observed biomass. Horizontal

blue lines indicate the surface and bottom of the ODZ, while the horizontal green line

indicates the base of the photic zone.

5

58
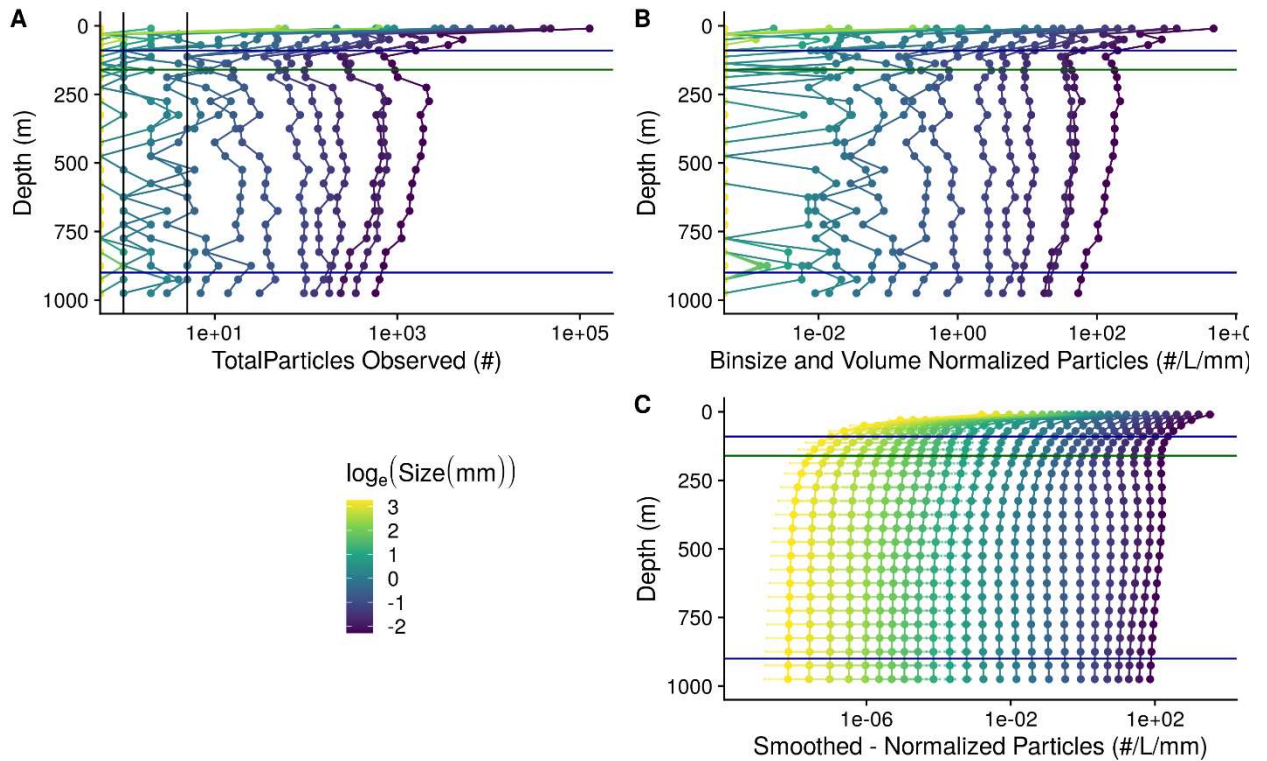
59   Figure S4. A profile of particle abundances at different sizes and depths, collected on

60   January 13 beginning at 06:13 at ETNP Station P2. Horizontal blue lines indicate the

61   surface and bottom of the ODZ, while the horizontal green line indicates the base of the

62   photic zone. (A) Numbers of observed particles. As the x axis is log transformed, zeros

63   are indicated as points along the Y axis. Vertical black lines indicate 1 and 5 observed

64   particles, respectively. (B) Particle numbers normalized to volume sampled and particle

65   size bin width. (C) Smoothed and extrapolated particle abundances, based on a negative

66   binomial GAM that predicts particle abundance form size and depth.

67
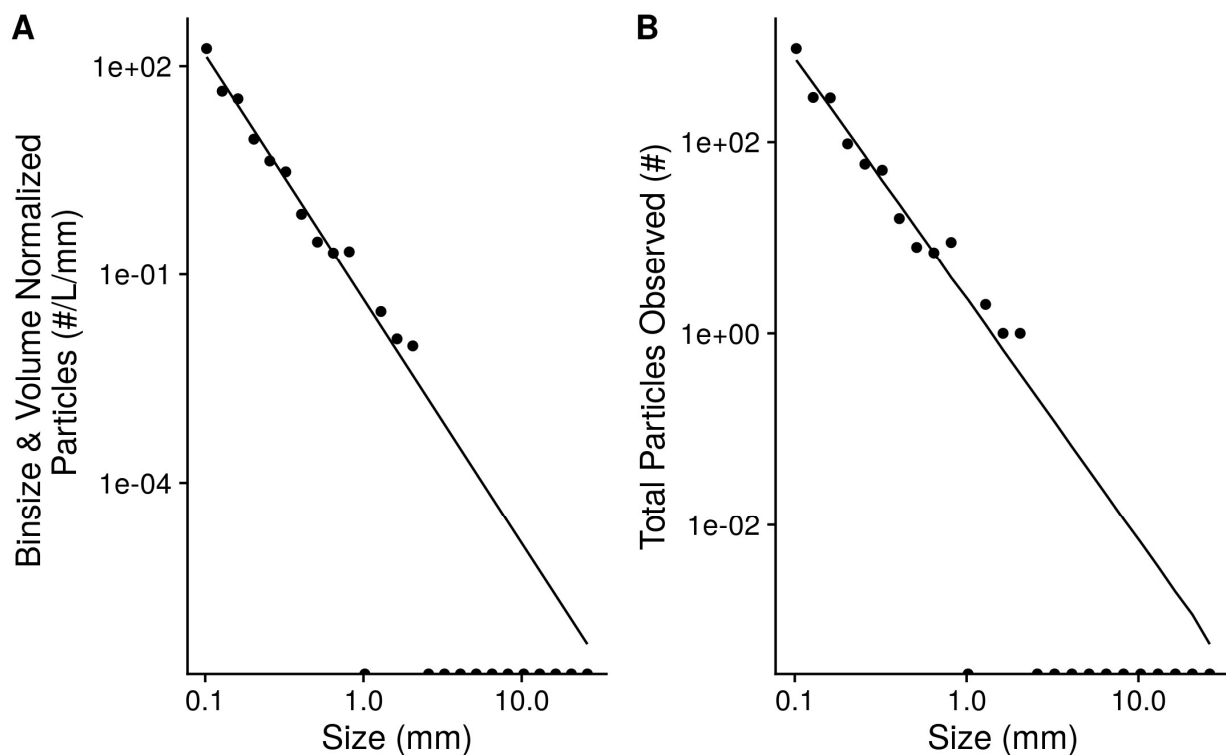
Figure S5. An example of observed particle size distribution spectra. These are depth

binned data from between 150 and 175 m deep in the water column from the cast that

occurred at *2017-01-13 17:51* local time at ETNP Station P2. This depth bin contains

total numbers of particles that were seen across 206.8 L of merged UVP image volume.

Points indicate (A) total numbers of observed particles and (B) particle numbers

normalized to volume sampled and particle size bin width. Half-dots along the x axis

correspond to particle size bins in which zero particles were observed. The line indicates

the predicted best fit line of the data. The line was fit on the binsize and volume

normalized data by a negative-binomial general linear model. The line in panel A

indicates predictions from this same model, re-scaled into absolute particle space.

78
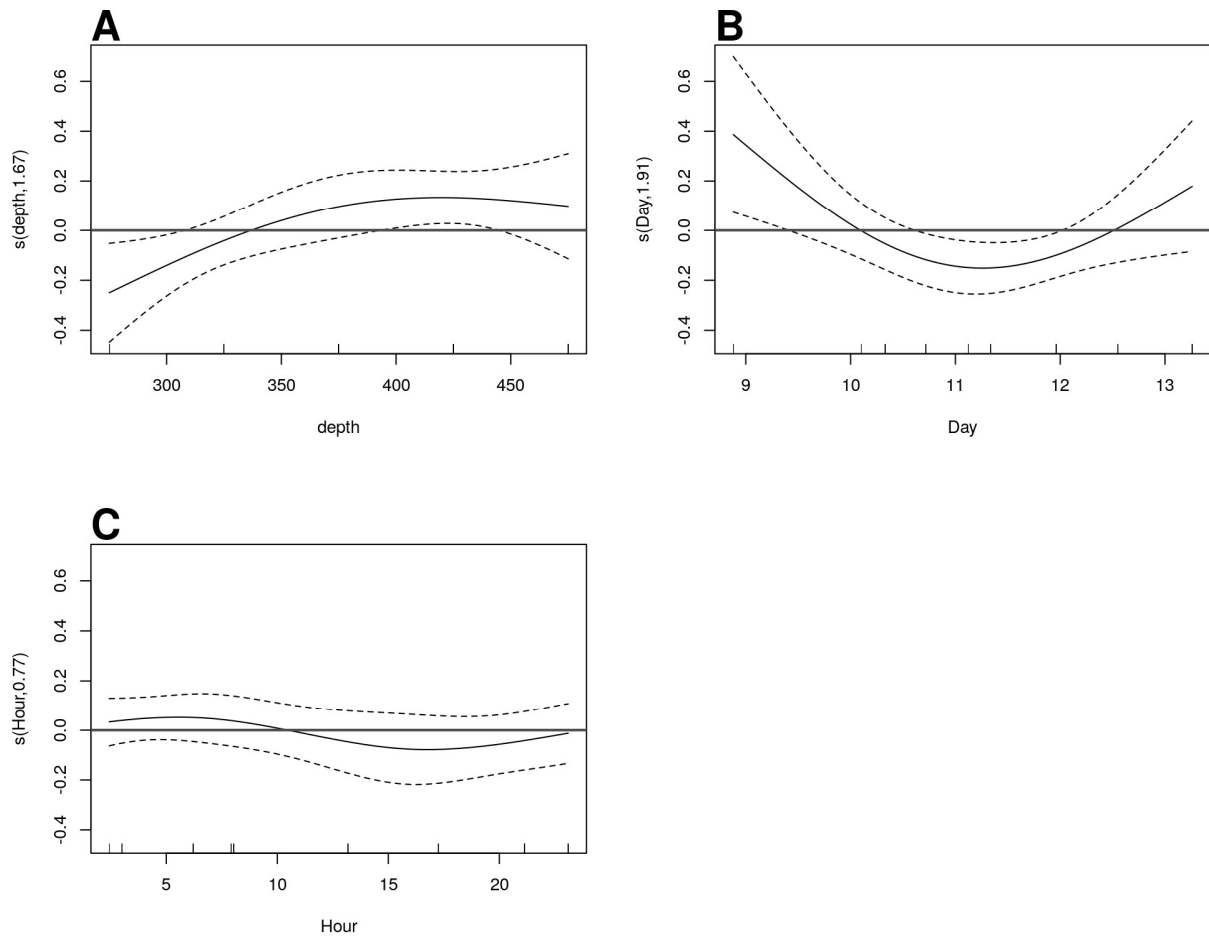
79   Figure S6. GAM predicted effects of A Depth, B Day of the month in January 2017, and

80   C hour of the day on the fifth-root transformed, depth normalized, rate of change of flux

81   at ETNP Station P2. Y axis indicates the value of the component smooth functions effect

82   on Flux. Positive values associate with times and regions of the water column where flux

83   is increasing, holding other factors constant, and negative ones where it is decreasing.

84   Horizontal gray line indicates y = 0, corresponding to that parameter having zero effect,

85   positive or on the outcome. Only Depth has a statistically significant relationship to rate

86   of change of flux (see section 6.5).
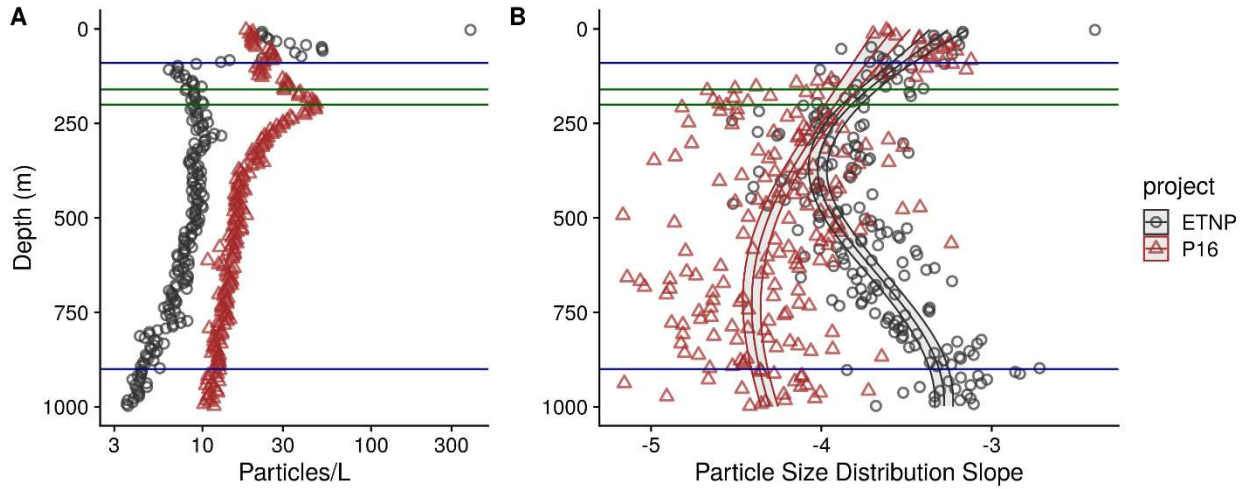
Figure S7. As above, but for the final cast taken at ETNP station P2 and the only cast collected from the P16 transect at Station 100. P16 Station 100 was chosen because it is at a similar latitude to ETNP station P2. (A) Total particle numbers, (B) Particle size distribution. Horizontal blue lines indicate the surface and bottom of the ODZ at the ETNP station, while the horizontal green lines indicate the bases of the photic zone at ETNP Station P2 (160m) and P16 Station 100 (200m).
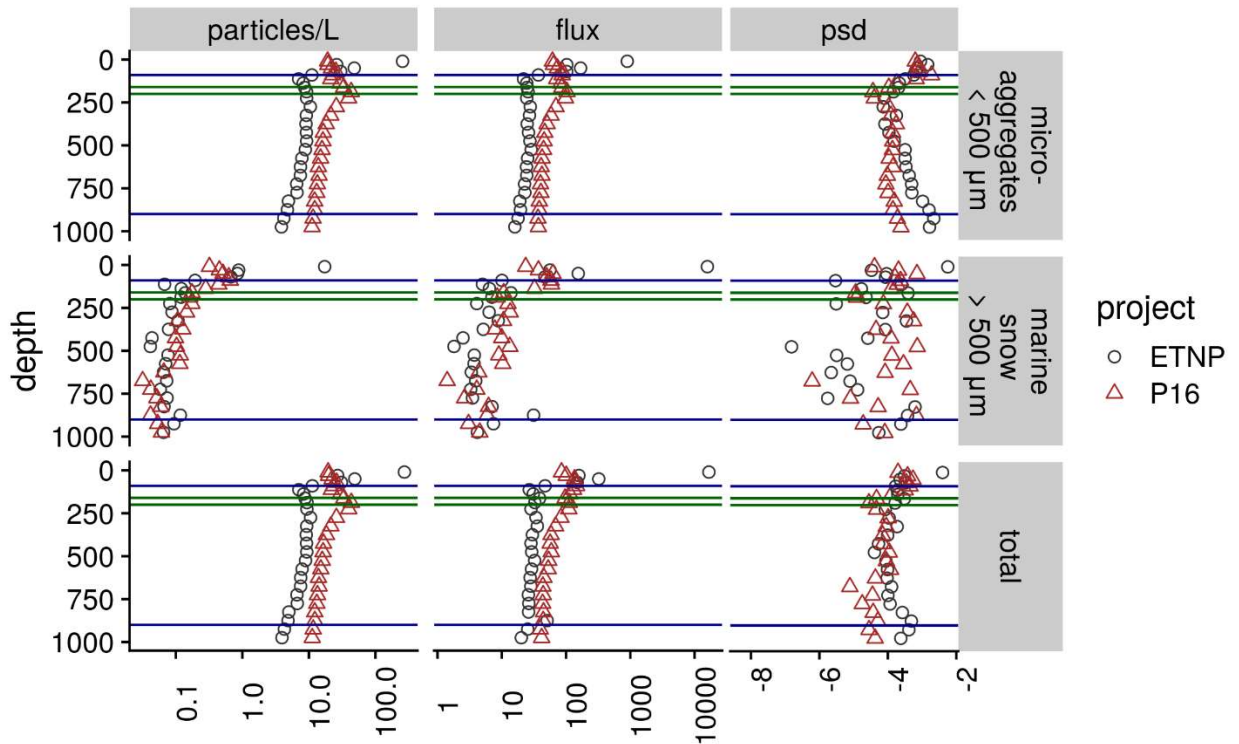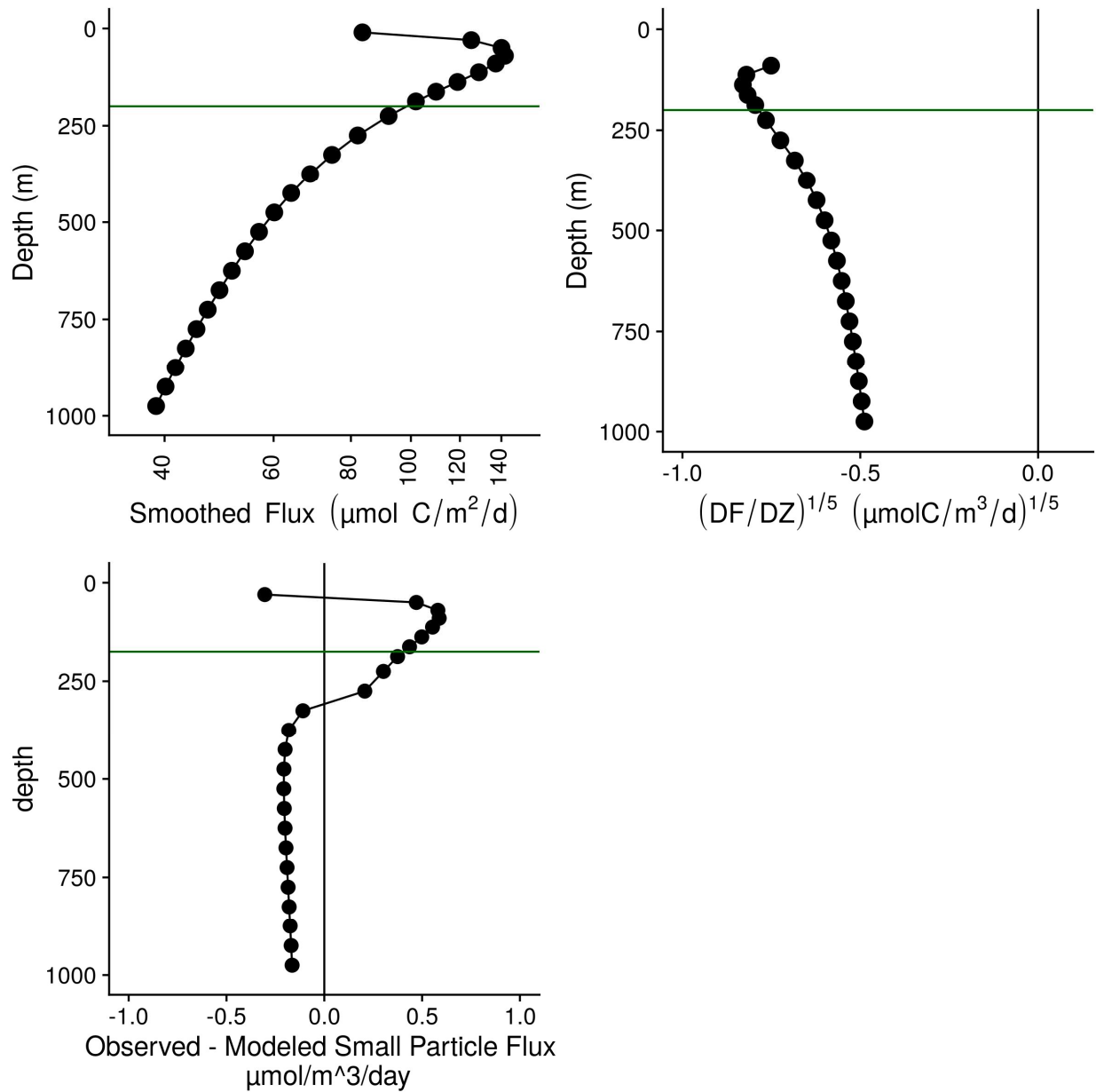
95
96   Figure S8. Depth binned particle number (volume normalized), particle size slope (PSD),

97   and flux (estimated as in Fig. 4) for microaggregates ($<= 500\,\mu m$), marine snow ($>$

98    $500\,\mu m$) and total particles, at the oxic (P16 Station 100) and anoxic site (ETNP Station

99   P2). Within each panel, horizontal blue lines indicate the surface and bottom of the ODZ

100   at the ETNP station, while the horizontal green lines indicate the bases of the photic zone

101   at ETNP Station P2 (160m) and P16 Station 100 (200m).

10

Figure S9. Flux profiles and flux attenuation at P16 Station 100. (A) Flux profile (B) Fifth-root transformed depth normalized rate of flux decrease. (C) Difference between observed and modeled results. Higher values suggest more disaggregation-like processes. The horizontal green line at 200 m indicates the base of the DCM as estimated by World Ocean Atlas data for this site.
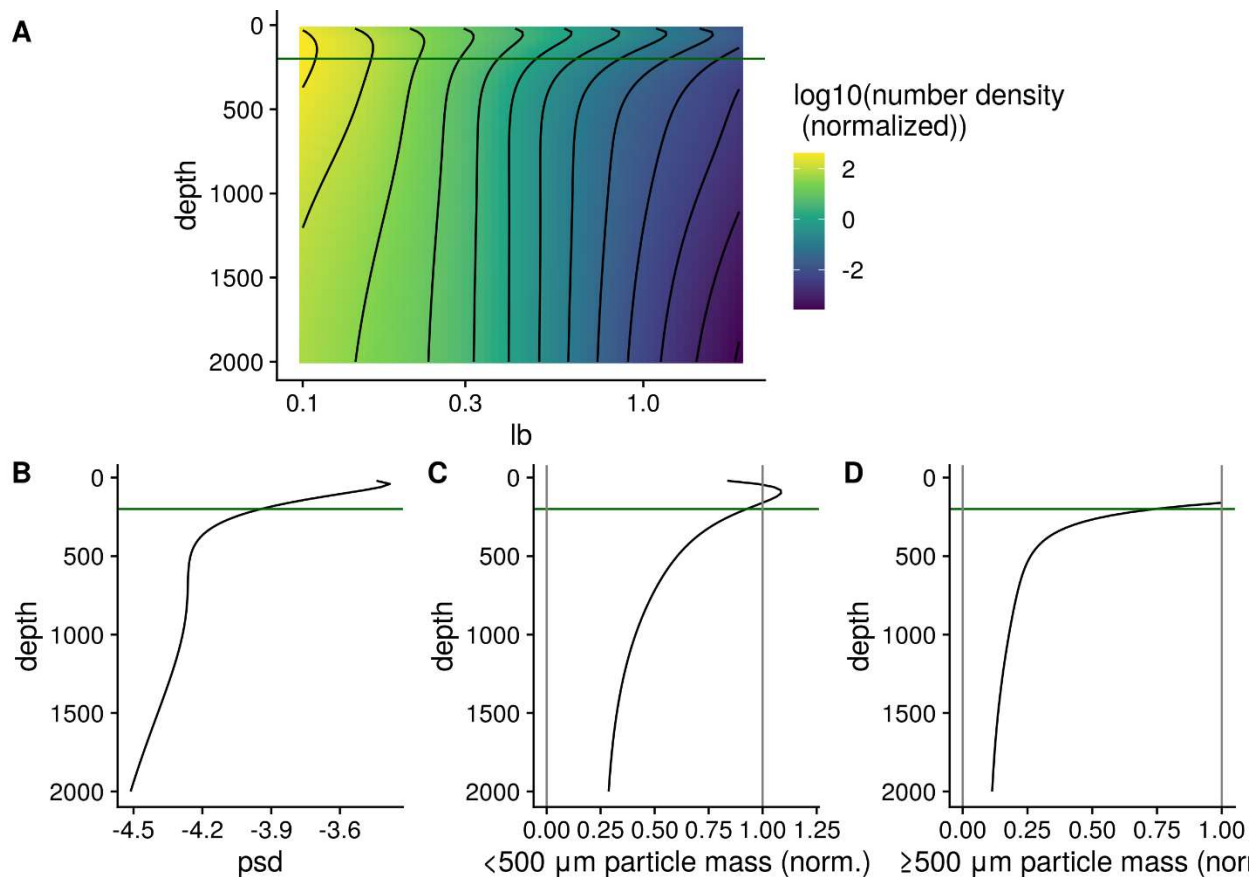
11

108
109　Figure S10. The same profiles as shown in Figure 5, but for the oxic site P16 Station

110　100. (A) GAM smoothed bin-size and volume particle numbers at each particle size class.

111　(B) Particle size distributions. And estimated biomass of (C) Small and (D) Large

112　particles. The horizontal green line at 200 m indicates the base of the DCM as estimated

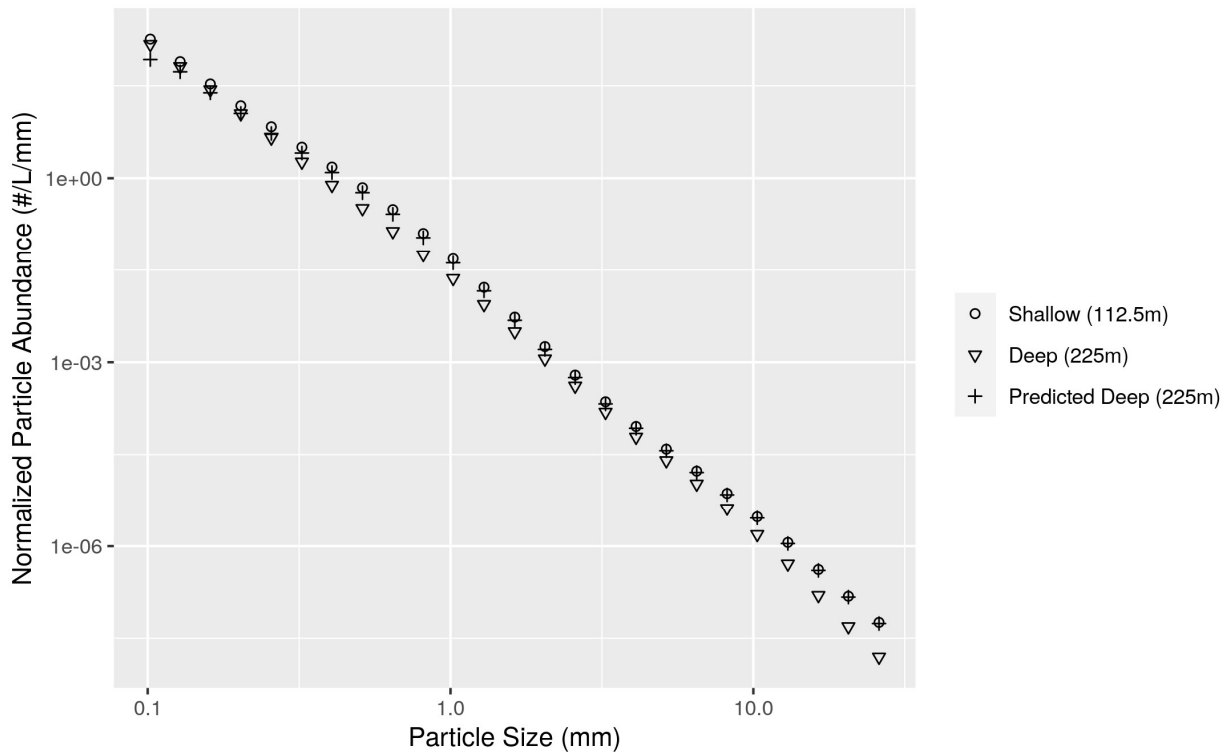113　by World Ocean Atlas data for this site.

12

114

Figure S11. An example of differences between modeled and observed particle slope.
The particle size distribution at a shallow and a deeper depth, from ETNP Station P2, are
shown. The model generates a prediction of the deep depth profile from the shallow
depth profile and the flux attenuation between the two profiles. The model predicts more
attenuation of the smallest particles than is actually observed. In practice the model
compares depths that are closer together than the two shown here. In particular, the depth
bin above 225m in our analysis has a midpoint of 187.5m, but we choose in this example
to compare the 225m particle size profile to the profile at 112.5 m. Two depths that are
far apart are shown so that the flux attenuation is large enough to be seen by eye and to
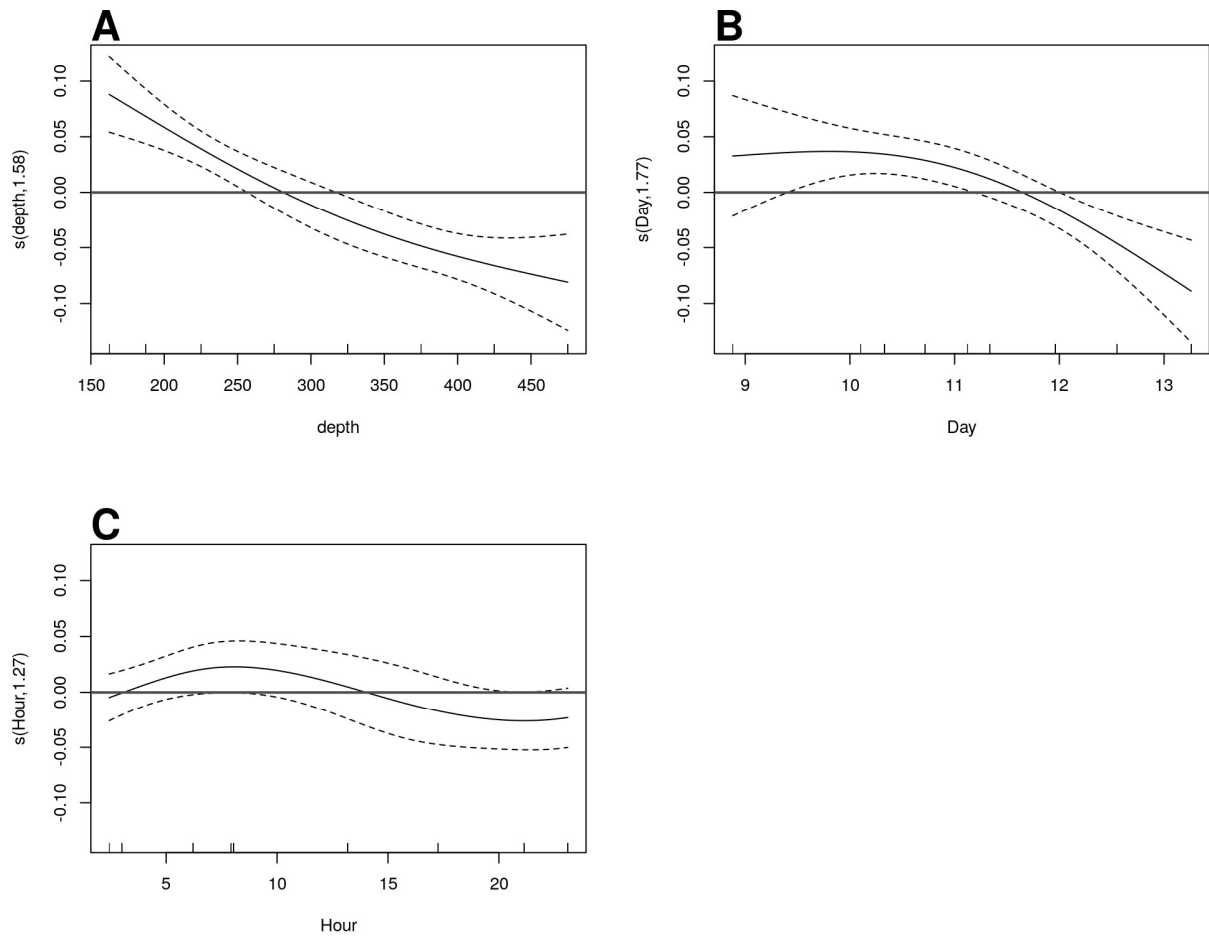provide a conceptual example of the models' function.

13

125

126　Figure S12. GAM predicted effects of A Depth, B Day of the month in January 2017, at

127　ETNP Station P2. Y axis indicates the value of the component smooth functions effect on

128　the difference between observed and modeled flux. Thus higher values correspond with

129　greater flux of small particles than predicted by the model. Horizontal gray line indicates

130　$y = 0$, corresponding to that parameter having zero effect, positive or on the outcome.

131　Only Depth and Day have a statistically significant relationship to rate of change of flux

132　(see Section 6.8).

133

134　Text S1. Full mathematical justification for the Eulerian version of the particle

135　remineralization and sinking model (PRiSM) model. Ful document uploaded separately.

14

Diagnosed Particle Disaggregation

Jacob A. Cram

May 21, 2021

1 Definitions and Units

$$m = C_m r^\alpha \tag{1}$$

As in DeVries et al. [2014] particle mass m is a function of radius r and scales with a fractal dimension α. C_m is a constant.

$$w = C_w r^\gamma \tag{2}$$

Sinking speed also scales with mass to another constant γ. According to Guidi et al. [2008] $\gamma = \alpha - 1$, but we'll keep things in terms of γ going forward.

$$F = nmw = nC_m C_w r^{\alpha+\gamma} \tag{3}$$

Flux F is a function of particle numbers, mass, and sinking speed.

Going forward we will determine the calculations for how many particles of size j in shallow depth i-1 remineralize into smaller particles of size j-1 in deeper depth i. We will call this term Δn_j

2 Conservation of particle number flux

In the absence of disaggregation, the number of particles leaving a box of water is equal to the number of particles going into that box from above. In other words, particle "number-flux" is conserved. Thus the number of particles in the box is a function of the number of particles going into that box, and the difference in velocities between when the particle enters and when that particle leaves.

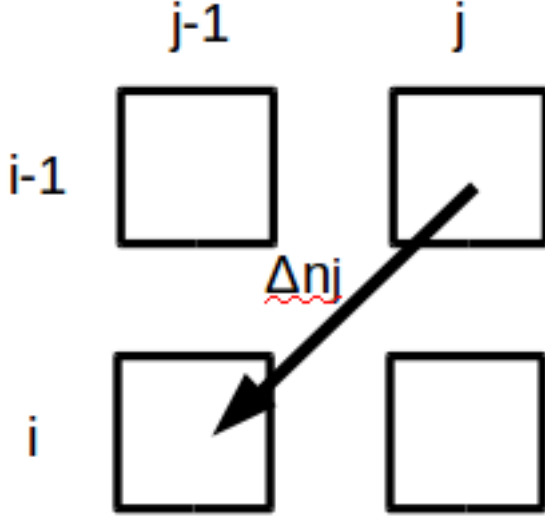$$n_{i-1,j-1}\frac{w_{j-1}}{w_j} + n_{i-1,j} = n_{i,j-1}\frac{w_{j-1}}{w_j} + n_{i,j} \tag{4}$$

Figure 1: Some number of particles Δn_j of size "j" remineralize to size "j-1" as they sink from depth "i-1" to depth "i".

Where $n_{i-1,j}$ is the number of particles of size j (the bigger size) at depth i-1 (the shallower depth). The subscripts correspond to locations in Figure 1.

We can re-arrange equation 4

$$n_{i-1,j-1}w_{j-1} + n_{i-1,j}w_j = n_{i,j-1}w_{j-1} + n_{i,j}w_j \tag{5}$$

Substitue in equation 2 into equation 5.

$$n_{i-1,j-1}r_{j-1}^{\gamma} + n_{i-1,j}r_j^{\gamma} = n_{i,j-1}r_{j-1}^{\gamma} + n_{i,j}r_j^{\gamma} \tag{6}$$

Rearrange equation 6

$$r_{j-1}^{\gamma}(n_{i-1,j-1} - n_{i,j-1}) = r_j^{\gamma}(n_{i,j} - n_{i-1,j}) = \Phi \tag{7}$$

Where Φ is a placeholder standing for either side of equation 7, which I will subsequently substitute into things.

Solve for Δn_j

$$\Delta n_j = n_{i,j} - n_{i-1,j} = \frac{r_{j-1}^{\gamma}}{r_j^{\gamma}}(n_{i-1,j-1} - n_{i,j-1}) \tag{8}$$

3 Conservation of Mass Flux

Total flux defined is the sum of flux in each (observed) particle size bin. Particles not in an observed bin don't count towards total flux.

$$\Delta F = \sum_{j=2}^{n} \Delta f_j + \Delta f_1 \tag{9}$$

Here Δf_j is the flux attenuation from bin of size j and Δf_1 is the loss that comes from particles in bin 1 becoming small enough that you can no longer see them with the UVP.

The flux attenuation in a bin is the product of the rate of flux attenuation with depth of each individual particle $\frac{\partial f}{\partial z}$, the depth interval over which the particles attenuate Δz and the number of particles in that bin at the top of the depth interval $n_{i-1,j}$

$$\Delta f_j = \frac{\partial f}{\partial z} \Delta z n_{i-1,j} \tag{10}$$

Furthermore, the rate of flux attenuation with respect to depth is the product of the rate of mass attenuation with respect to time $\frac{\partial m}{\partial t}$, the inverse of the sinking speed $\frac{\partial t}{\partial z}$, and the deriviative of the flux to mass relationship $\frac{\partial f}{\partial m}$.

$$\frac{\partial f}{\partial z} = \frac{\partial m}{\partial z} \frac{\partial f}{\partial m} = \frac{\partial m}{\partial t} \frac{\partial t}{\partial z} \frac{\partial f}{\partial m} \tag{11}$$

In PRiSM, fractional mass loss as a function of time is the same for all particles of all sizes.

Now we are going to come up with the values for each of these terms.

The particle remineralization rate C_r is the same for particles of all sizes.

$$\frac{\partial m}{\partial t} = C_r * m = C_r C_m r^\alpha \tag{12}$$

Sinking speed definition, substituting from equation 2

$$\frac{\partial t}{\partial z} = \frac{1}{w} = \frac{1}{C_w r^\gamma} \tag{13}$$

Flux for a given size class, substituting eqation 1, and finally putting everything in terms of mass (rather than mass and radius, since the two are related)

$$f = mw = m * C_w r^\gamma = m * C_w (\frac{m}{C_m})^{\frac{\gamma}{\alpha}} \tag{14}$$

Derriving equation 14 with respect to mass, and substituting equation 1

$$\frac{\partial f}{\partial m} = Cw(1 + \frac{\gamma}{\alpha})(\frac{m}{C_m})^{\frac{\gamma}{\alpha}} = C_w(1 + \frac{\gamma}{\alpha})r^\gamma \tag{15}$$

Finally, we can construct our equation for flux attenuation by substituting equations 12, 13 and 15 into equation 11

$$\frac{\partial f}{\partial z} = C_r C_m r^\alpha (1 + \frac{\gamma}{\alpha}) \tag{16}$$

And now we can solve for equation 17.

$$\Delta f_j = C_r C_m r^\alpha (1 + \frac{\gamma}{\alpha})\Delta z * n_{i-1,j} \tag{17}$$

We also need to solve for Δf_1 the flux "attenuation" that actually comes from particles leaving the smallest bin and escaping from what the UVP sees.

$$\Delta f_1 = \Delta n_1 m_1 w_1 = \Delta n_1 C_m C_w r_1^{\alpha+\gamma} \tag{18}$$

Here, Δn_1 is the number of particles leaving bin j = 1, but we haven't solved for that yet.

4 Solving for Δn_j

Recall that Δn_j is the number of particles that migrate between bin "j" and bin "j-1" as the particles sink from depth "i-1" to depth "i".

The flux at the shallower depth is equal to the flux at the deeper depth, plus the flux that attenuated between those two depths. Since $f = nmw$ and we know m and w

$$n_{i-1,j-1}C_m C_w r_{j-1}^{\alpha+\gamma} + n_{i-1,j}C_m C_w r_j^{\alpha+\gamma} = n_{i,j-1}C_m C_w r_{j-1}^{\alpha+\gamma} + n_{i,j}C_m C_w r_j^{\alpha+\gamma} + \Delta f_j \tag{19}$$

This equation can be re-arranged, and we can substitute in equation 17 for Δf_j.

The C_m cancel out.

$$C_w r_{j-1}^{\alpha+\gamma}(n_{i-1,j-1} - n_{i,j-1}) = C_w r_j^{\alpha+\gamma}(n_{i,j} - n_{i-1,j}) + C_r(1 + \frac{\gamma}{\alpha})\Delta z n_{i-1,j} r^\alpha \tag{20}$$

We can then substitute in Φ from equation 7.

$$C_w r_{j-1}^\alpha \Phi = C_w r_j^\alpha \Phi + C_r(1 + \frac{\gamma}{\alpha})\Delta z n_{i-1,j} r^\alpha \tag{21}$$

4

Rearrange

$$C_w\Phi(r_{j-1}^\alpha - r_j^\alpha) = Cr(1 + \frac{\gamma}{\alpha})\Delta z r^\alpha n_{i-1,j} \tag{22}$$

solve for Φ

$$\Phi = \frac{\frac{C_r}{C_w}\Delta z r^\alpha n_{i-1,j}(1 + \frac{\gamma}{\alpha})}{r_{j-1}^\alpha - r_j^\alpha} \tag{23}$$

$$\Delta n_j = \frac{\Phi}{r_j^\gamma} = \frac{\frac{C_r}{C_w}\Delta z r^\alpha n_{i-1,j}(1 + \frac{\gamma}{\alpha})}{r_j^\gamma(r_{j-1}^\alpha - r_j^\alpha)} \tag{24}$$

$$\Delta n_{j-1} = \frac{\Phi}{r_{j-1}^\gamma} = \frac{\Delta n_j r_j^\gamma}{r_{j-1}^\gamma} \tag{25}$$

At this point, the only unsolved variable is C_r, which we can now calculate.

5 Solving for C_r

We can calculate ΔF, the attenuation of flux and can impose the size spectrum and all of the other constants. Here we find the C_r that gives us the correct ΔF

First, to solve equation 9 by substituting in equaitons 17 and 18

$$\Delta F = \sum_{j=2}^n \Delta f_j + \Delta f_1 = \sum_{j=2}^n \left\{ C_r C_m r_j^\alpha (1 + \frac{\gamma}{\alpha})\Delta z n_{i-1,j} \right\} + \Delta n_1 C_m C_w r_1^{\alpha+\gamma} \tag{26}$$

Substitute equation 24 for Δn_j when j = 1 for Δn_1

$$\Delta F = \sum_{j=2}^n \Delta f_j + \Delta f_1 = \sum_{j=2}^n \left\{ C_r C_m r_j^\alpha (1 + \frac{\gamma}{\alpha})\Delta z n_{i-1,j} \right\} + \frac{\frac{C_r}{C_w}\Delta z r_1^\alpha n_{i-1,1}(1 + \frac{\gamma}{\alpha})}{r_1^\gamma(r_0^\alpha - r_1^\alpha)} C_m C_w r_1^{\alpha+\gamma} \tag{27}$$

In the above, r_0 is the effective size of the particles smaller than the UVP can see. In principle this is arbitrary. Numbers closer to zero result in fewer particles in the smallest bin disapearing, larger ones to more of those particles disapearing. As r_0 approaches r_1 Cr approaches zero. They cannot be equal or the math breaks.

Pull what I can out of the sum operation, and cancel out r^γ and C_w from the rightmost term

$$\Delta F = C_r C_m \Delta z (1 + \frac{\gamma}{\alpha}) \sum_{j=2}^{n} \left\{ r_j^\alpha n_{i-1,j} \right\} + \frac{C_r \Delta z r_1^{2\alpha} n_{i-1,1} (1 + \frac{\gamma}{\alpha})}{(r_0^\alpha - r_1^\alpha)} C_m \quad (28)$$

Now we can solve for C_r

$$C_r = \frac{\Delta F}{C_m \Delta z (1 + \frac{\gamma}{\alpha}) \left[\sum_{j=2}^{n} \left\{ r_j^\alpha n_{i-1,j} \right\} + \frac{r_1^{2\alpha} n_{i-1,1}}{r_0^\alpha - r_1^\alpha} \right]} \quad (29)$$

Thus for a pair of profiles, we can estemate the flux attenuation, calculate Cr from that, and then plug Cr (and the profile) into the equation 24 for Δn_j. We can thus compute Δn_j for each size class to see how many particles from that bin move to the next bin smaller.